Deep-water sediment transport patterns and basin floor topography in early rift basins: Plio-Pleistocene syn-rift of the Corinth Rift, Greece

Martin Muravchik[1], Gijs A. Henstra[1], Gauti T. Eliassen[1], Rob L. Gawthorpe[1], Mike Leeder[2], Haralambos Kranis[3], Emmanuel Skourtsos[3] & Julian Andrews[2]

1. Department of Earth Science, University of Bergen, Bergen, Norway
2. School of Environmental Sciences, University of East Anglia, Norwich, United Kingdom
3. Faculty of Geology and Geoenvironment, University of Athens, Athens, Greece

ABSTRACT

Our current understanding on sedimentary deep-water environments is mainly built of information obtained from tectonic settings such as passive margins and foreland basins. More observations from extensional settings are particularly needed in order to better constrain the role of active tectonics in controlling sediment pathways, depositional style and stratigraphic stacking patterns. This study focuses on the evolution of a Plio-Pleistocene deep-water sedimentary system (Rethi-Dendro Formation) and its relation to structural activity in the Amphithea fault block in the Corinth Rift, Greece. The Corinth Rift is an active extensional basin in the early stages of rift evolution, providing perfect opportunities for the study of early deep-water syn-rift deposits that are usually completely eroded from the rift shoulders due to erosion in mature basins like the Red Sea, North Sea and the Atlantic rifted margin. The depocentre is located at the exit of a structurally-controlled sediment fairway, approximately 15 km from its main sediment source and 12 km basinwards from the basin margin coastline. Fieldwork, augmented by digital outcrop techniques (LiDAR and photogrammetry) and clast-count compositional analysis allowed identification of 16 stratigraphic units that are grouped into six types of depositional elements: A - mudstone-dominated sheets, B - conglomerate-dominated lobes, C - conglomerate channel belts and sandstone sheets, D - sandstone channel belts, E - sandstone-dominated broad shallow lobes, F - sandstone-dominated sheets with broad shallow channels. The formation represents an axial system sourced by a hinterland-fed Mavro delta, with minor contributions from a transverse system of conglomerate-dominated lobes sourced from intrabasinal highs. The results of clast compositional analysis enable precise attribution for the different sediment sources to the deep-water system and their link to other stratigraphic units in the area. Structures in the Amphithea fault block played a major role in controlling the location and orientation of sedimentary systems by modifying basin-floor gradients due to a combination of hangingwall tilt, displacement of faults internal to the depocentre and folding on top of blind growing faults. Fault activity also promoted large-scale subaqueous landslides and eventual uplift of the whole fault block.

INTRODUCTION

Most of the present day knowledge on sedimentary deep-water environments originates from studies located at passive margins (e.g., Wynn *et al*., 2002; Gee *et al*., 2007; Deptuck *et al*., 2007; Armitage *et al*., 2012; Aspiroz-Zabala *et al*., 2017), foreland basins (e.g., Winn & Dott, 1977; Johnson *et al*., 2001; Hodgson *et al*., 2006; Hubbard *et al*., 2008; Fildani *et al*., 2013) and the offshore California strike-slip basins (e.g., Normark, 1978; Carvajal *et al*., 2017; Symons *et al*., 2017). Information obtained from extensional basins is relatively small (e.g., Ferentinos *et al*., 1988; Papatheodorou & Ferentinos, 1993; Ravnås & Steel, 1997; Leeder *et al*., 2002; Leppard & Gawthorpe, 2006; Jackson *et al*., 2011; Strachan *et al*., 2013; Zhang *et al*., 2014; Zhang & Scholz, 2015; Henstra *et al*., 2016; McArthur *et al*., 2016), especially on aspects like rock body geometries, sediment pathways and their interaction with evolving depocentre structures.

The compartmentalized nature of extensional basins plays a crucial role in determining the dimensions and geometry of deep-water sedimentary rock bodies as well as their orientation and stacking patterns. This is because the uplift and subsidence generated by extensional tectonics creates vertical offsets in the order of thousands of meters occurring at a fault-block scale (usually between 10 to 30 km in length; e.g., Cowie *et al*., 2000; Gawthorpe & Leeder, 2000; Ziegler & Cloething, 2004). The resulting strong topographic gradients evolve with time and determine source and sink areas in the rift, with the possibility of multiple sources of sediment, including the rift shoulder and intra-rift fault blocks operating at the same time. Axial and transverse drainage in deep-water extensional basins are widely recognised features (e.g., Papatheodorou & Ferentinos, 1993; Smith & Busby, 1993; Zhang *et al*., 2014; Zhang & Scholz, 2015; McArthur *et al*., 2016), often included in rift basin sedimentary models (e.g., Leeder & Gawthorpe, 1987; Ravnås & Steel, 1998; Gawthorpe & Leeder, 2000). Nevertheless, studies on deep-water syn-rift deposits tend to concentrate on the processes occurring on the subaqueous slope systems associated with marginal basin fault scarps (e.g., Ferentinos *et al*., 1988; Leeder *et al*., 2002; Leppard & Gawthorpe, 2006; Strachan *et al*., 2013; Henstra *et al*., 2016) and more rarely, on the deposits sourced from hangingwall dipslopes (e.g., Ravnås & Steel, 1997; Jackson *et al*., 2011). The present study addresses the need for linkage of the various parts of deep-water sedimentary systems in rift basins and analyses their evolution in conjunction with normal fault growth, the role of intrabasinal highs as sediment sources and structural control of basin floor gradients. Addressing such issues has important impact on rift basin studies in general, for the understanding of deep-water drainage behaviour and also their application to subsurface exploration and production.

This study focuses on the evolution of a deep-water sedimentary system and its interaction with the extensional structures in a rift axis depocentre located approximately 12 km basinwards of the contemporaneous margin coastline and at the exit of a structurally controlled sediment fairway, ~15 km along-strike of its deltaic sediment source. The studied deposits are the Plio-Pleistocene Rethi-Dendro Formation (hereafter RDF) exposed in the Amphithea fault block, Corinth Rift, Greece (Fig. 1). The study of deep-water deposits in extensional settings is often a challenge because the deposits tend to be buried in the subsurface. In contrast, the Corinth Rift represents one of a very few basins in the world where early syn-rift deposits are presently exposed due to uplift of the rift shoulder without any inversion of the extensional structures. This represents nearly unique conditions for the study of the original geometry of deep-water deposits and their link to the structural evolution of a rift depocentre. Moreover, the Corinth Rift is an active extensional basin still in the relatively early stages of rift evolution. Consequently, this study offers important insights into the development of early rift deep-water deposits that are usually completely eroded from the rift shoulders in more mature basins such as the Red Sea, North Sea and the Atlantic rifted margin in general (e.g. Steckler *et al*., 1988; Nøttvedt *et al*., 2000; Ravnås *et al*., 2000; Bosworth *et al*., 2005; Torsvik *et al*., 2009; Moulin *et al*., 2010).

GEOLOGICAL SETTING

The Corinth Rift originated ~5 Ma from N-S extension occurring between the North Anatolian fault and the Kephalonia fault/Hellenic subduction zone (Collier & Dart, 1991; Leeder *et al*., 2008) and cuts across the N-S striking Hellenide thrust belt (Fig. 1). The rift structure is characterised by mainly E-W striking normal fault segments up to 20 km in length, that mainly dip towards the north and can achieve several kilometres of displacement. Fault activity in the rift progressively migrated from S to N with present-day extension concentrated on the fault network developed along the southern coast of the Gulf of Corinth. Activity of the rift is characterised by two main phases (Gawthorpe *et al*., 2017b): Rift 1 from 5.0–3.6 to 2.2–1.8 Ma and Rift 2 from 2.2–1.8 Ma to present. Rift 1 is exposed mainly on the southern margins of the Corinth Gulf and represents the evolution from fluvial and palustrine conditions during rift initiation to the establishment of a deep-water lake as the creation of accommodation progressed. At the onset of Rift 2, fault activity shifted towards the north, causing the subsequent uplift and erosion of the fault blocks that were active during Rift 1. The oldest extensional structures are found fossilized along the northern Peloponnese up to 30 to 40 km south of the modern southern shoreline of the Gulf of Corinth.

The pre-rift stratigraphy in the central Corinth rift area (Fig. 1) corresponds to the nappe units of the Hellenide thrust belt. From structurally deeper to shallower levels, these are: 1) the Phyllites-Quartzites Unit, with high-pressure mica schists, phyllites, quartzites and rare metabasalts; 2) the Tripolis Unit, which comprises a dolomitised Upper Triassic to Upper Eocene shelf carbonate sequence and an Upper Palaeozoic to Lower Triassic volcano-sedimentary complex at the base (Tyros beds), capped by Lower Eocene to Oligocene flysch; and 3) the Pindos Unit, mainly formed of Mesozoic pelagic limestones and chert with volcanic and clastic rocks at the base and Paleocene to Eocene flysch sequences towards the top (e.g., Pe-Piper & Piper, 1991; Skourtsos *et al*., 2016).

Rifting is interpreted to have started in the latest Miocene or early Pliocene based on radiometric dating (Collier & Dart, 1991; Leeder *et al*., 2008) and the syn-rift succession in the central Corinth rift has been subdivided by Gawthorpe *et al.* (2017b) into the following stratigraphic units, from base to top: the fluvial Korfiotissa Formation, the floodplain to palustrine Ano Pitsa Formation, the lower slope to pro-delta Pellini Formation, the lacustrine RDF and the laterally equivalent Kefalari, Kyllini, Mavro, Evrostini and Illias deltas, unconformably overlain by the Kryoneri delta, Pleistocene marine terraces, tufas and deltas and present-day sedimentary systems (Fig. 1). The RDF in the Amphithea fault block is the focus of this study. However, the RDF and similar rock units have been mapped together through several fault blocks (Tataris *et al*., 1970; Bornovas *et al*., 1972; Koutsouveli *et al*., 1989; Tsoflias *et al*., 1993) that were active at different times during both Rift 1 and Rift 2 with ages between late Pliocene to middle Pleistocene (see Gawthorpe *et al*., 2017b).

The Amphithea fault block

The present-day structural configuration of the Amphithea fault block is mainly defined by the presence of two intrabasinal highs (the Amphithea and Xylokastro horsts) and a south-dipping fault lying in the subsurface close to the coast towards the north. This fault is interpreted to be the continuation of the Melissi fault exposed to the southeast of the city of Xylokastro (Gawthorpe *et al*., 2017b) (Figs 1 and 2). The hangingwall consistently dips towards the northeast where more than 1300 m of the RDF are exposed in continuous cliff sections on the western margin of the Sythas Valley. The base of the RDF is not exposed in this fault block and its top is eroded by an angular unconformity developed at the base of a complex of down-stepping Pleistocene delta lobes and marine terrace deposits (Gawthorpe *et al*., 2017b). The normal faults in the hangingwall have a NE-SW orientation, parallel to the Koutsa fault at the southeastern border of the Xylokastro Horst and highly oblique to perpendicular to the northern and southern boundary fault systems of the Amphithea fault block (Figs 1 and 2). The smaller-scale fault blocks within the Amphithea area are designated as Fault Blocks 1, 2, 3, 4 and 5 (Fig. 2).

The horst configuration of the Amphithea and Xylokastro intrabasinal highs is a recent feature that was not fully developed during deposition of the RDF in the Amphithea fault block (Gawthorpe *et al*., 2017b). The Koutsa and Melissi fault planes were exposed during the deposition of RDF in the study area, but the Amphithea fault is interpreted to have been buried and, by propagating-upwards, has created a syn-sedimentary forced-fold (Gawthorpe *et al*., 2017b). The normal faults in the hangingwall have a throw that varies from approximately 20 to 70 m. Differences in thickness across these faults indicate that they were active during the deposition of the RDF (Figs 2 and 3).

METHODOLOGY

Field-based study involved analysis of exposures 100 to 250 m high in near-vertical cliffs of the western margin of the Sythas Valley (Figs 2 and 3). This was achieved by detailed field mapping and sedimentary logging, combined with 3D digital outcrop analysis acquired from terrestrial LiDAR, photogrammetry and UAV mapping techniques. This approach allowed the integration of small and large scale observations into one common group of digital outcrop models that was subsequently interpreted with the aid of Virtual Reality Geological Studio software (VRGS, e.g. Hodgetts, 2009; Rarity *et al.*, 2014). By these means, measurements from bed to fault block scale of bedding and rock body orientation and the dimensions and orientation of unit boundaries were obtained. The analysis of bedding measurements at fault block scale allowed for the detection of angular unconformities within the stratigraphy of the RDF (Fig. 4) and the effect of basin-floor tilting in the evolution of the subaqueous environment (e.g., Ravnås & Steel, 1997; Muravchik *et al.*, 2017).

In order to identify sediment sources for the different deposits in the RDF, clast composition counts were performed on conglomerate-grade beds within this formation and its surrounding stratigraphic units. The method involves registering the composition of the clasts along a regular matrix in which node spacing is defined by the mean clast size of the bed under scrutiny (Muravchik *et al.*, 2014). Percentage pie charts (Fig. 1) and spider diagrams (Fig. 5) are used to illustrate the analysis and the complete dataset is presented as Supplementary data.

Analysis of the orientation of the sedimentary systems in the RDF is mainly based on measurements of rock body orientation such as lobe axes and channel thalwegs (e.g. Fabuel-Pérez *et al.*, 2009; Muravchik *et al.*, 2014; Rarity *et al.*, 2014) from the digital outcrop models (Fig. 6). Measurements were complemented by palaeocurrent directions obtained from logged sections (e.g. current ripples and trough-cross stratification). In order to better evaluate the significance of each directional feature, all measurements were weighted according to their size (cross sectional area in m^2; Fig. 6d).

THE RETHI-DENDRO FORMATION IN THE AMPHITHEA FAULT BLOCK

Deposition of the RDF in the Amphithea fault block occurred during Rift 1 in a deep-water lacustrine environment (Gawthorpe *et al.*, 2017b). There is no evidence for a connection with a marine basin and no sequence stratigraphic framework exists. Sixteen stratigraphic units are recognised in this study for the lower half of the formation based on rock body geometry, dimensions, internal architecture, grain size distribution and boundaries (Figs 2 and 3). The upper half of the formation consists of a series of slide sheets of NE vergence, composed of slices of units 14 and 16 (Figs 2a, b and 3). Although the exact age of the formation is not known, the 2.55 Ma age of an ash bed close to the base of Unit 16 (Leeder *et al.*, 2012) means that the Pliocene-Pleistocene boundary probably lies within Unit 14 (Fig. 3).

Tilting of the hangingwall in the Amphithea fault block occurred mainly towards the NNE, as it is revealed by the consistent dip direction of the RDF strata in that same direction (Fig. 2). Analysis of the angular unconformities within the RDF and differences in bedding dip values reveal the existence of discrete basin-floor tilting events of varying magnitude (Fig. 4) that are documented from the following three cases: 1) rotation of a monocline limb associated to the Amphithea fault (Fig. 4b, c); 2) an angular unconformity of ~8° (Fig. 4d) and 3) an angular unconformity of ~6° (Fig. 4d, e, f). Evidence for the rotation of the monocline limb associated to the Amphithea fault lie in a series of spatially restricted progressive angular unconformities that result from fanning geometries recorded within Unit 1 strata. These are found within the first 500 m of the hangingwall of the Amphithea fault in Fault Block 4 (between points 1 and 4 in Figs 2a and 3). The exposures display thickening of stratal packages down-dip the monocline limb (Fig. 4b) and conversely, subtle onlap stratal terminations up-dip onto the monocline limb (expanded view in Fig. 4b). Growth strata dip towards the NNE with the magnitude of dip decreasing consistently upwards and away from the Amphithea fault (Fig. 4b, c). This configuration is interpreted to indicate that the fault was a blind growth fault with a monocline flexure developed on top (Gawthorpe *et al.*, 2017b). The ~8° unconformity occurs within Unit 1, between the positions marked by the lobes of units 5 and 6 (Figs 2c, 3 and 4d). As this unconformity is only exposed in Fault Block 1 (Fig. 4d), it is not possible to assess its actual spatial extent. However, its NNE dip direction, almost coincident with the ~6° unconformity in Fault Block 1 (Fig. 4d), suggests its origin related to the tilting of the Amphithea hangingwall towards the northern boundary fault system. The ~6° unconformity is found at the base of Unit 11 and can be traced from Fault Block 1 to 4 (Figs 2b, c, 3 and 4d, e, f). The occurrence of the ~6° unconformity at exactly the same stratigraphic position in fault blocks 1, 2, 3 and 4 indicates that the process behind its origin was of a larger scale than these normal faults and is interpreted to have been linked to the tilting of the Amphithea fault block as a whole (Figs 2 and 4a, d, e, f). Variations in the orientation of the ~6° unconformity measured between fault blocks 1, 2 and 4 (Fig. 4d, e, f), result from the competing effect of backtilting faults of different orientations (i.e. Melissi fault vs. internal normal faults), showing that the internal normal faults were active during its development, as it is suggested by the differences in thickness of the unit immediately above the unconformity (Unit 11) between Fault Blocks 1, 2, 3 and 4 (Figs 2 and 3). The fact that the different depositional units in the formation consistently dip towards the NNE, together with the decrease in the magnitude of the dip of the bedding and angular unconformities upwards in the stratigraphy of the RDF (Figs 2 and 4) implies that tilting towards the northern boundary fault system at hangingwall scale was a first order control in the evolution of the depocentre (e.g., Ravnås & Steel, 1997; Muravchik *et al.*, 2017) and that the internal normal faults played a more local role (Figs 2a, c and 4).

The stratigraphic interval below the ~6° unconformity is characterised by more than 350 m of mudstone-dominated deposits represented by Unit 1, punctuated by the conglomerate-dominated lobes of units 2, 4, 5, 6 and 9 (Figs 2 and 3). Laterally equivalent to these units there is a channel system composed of units 3, 7, 8 and 10, which reaches 250 m at its thickest, close to the locality of Riza (Figs 2 and 3), where it was mapped as the Riza Member by Gawthorpe *et al.* (2017b). Units 8 and 10 in the channel system thin and interdigitate with Unit 1 towards the west (Figs 2 and 3), above the ~8° unconformity. The lateral relationship between Unit 1 and the channel system below the ~8° unconformity is less clear due to the nature of the exposures. Above the ~6° unconformity, the formation is characterised by the alternation of mudstone-dominated units (11 and 14) with intercalated conglomerate-dominated lobes (units 12 and 15) on the one hand and sandstone-dominated units (13 and 16) on the other (Figs 2 and 3).

Clast composition

The RDF and its laterally equivalent deposits are the oldest to contain metamorphic clasts derived from the lowest exposed structural levels of the Hellenide thrust belt, the Phyllites-Quartzites Unit, reflecting the progressive uplift and erosion of the rift shoulder (e.g. Rohais *et al*., 2007; Gawthorpe *et al*., 2017b). Gawthorpe *et al.* (2017b) suggested the Mavro delta as the source of the RDF in the Amphithea fault block based on the relative abundance of phyllite clasts in both units and their location and stratigraphic position. Closer inspection, however, reveals two clear compositional patterns. The main bulk of the deposits have a signature compatible with a mixed provenance from the Phyllites-Quartzites Unit, the Pindos Unit and the Tripolis Unit in the pre-rift. However, the conglomerate-dominated lobes of units 2, 4, 5, 6, 9, 12 and 15 (Fig. 3) contain granitoid clasts that are completely absent from the other RDF depositional units.

In order to better constrain the provenance of the deposits and assess the contribution of potentially multiple sediment sources, clast composition analyses were performed on selected RDF depositional units, on the closest delta units to the Amphithea fault block (i.e. Kyllini, Kefalari and Mavro, Fig. 1) and on early rift deposits exposed on the Amphithea and Xylokastro horsts (Fig. 1). The different compositions detected fall in the following categories: 1) limestone, sandstone and conglomerate clasts sourced from the Pindos and Tripolis units; 2) red chert, black chert and granitoid clasts sourced from the Pindos Unit and 3) phyllite, low grade metamorphic rock, microcrystalline quartz and quartzite clasts sourced from the Phyllites-Quartzites Unit (Fig. 5 and Supplementary data). It is important to note that the granitoid lithologies in the Pindos Unit are clasts in conglomerates found in the flysch and no other granitoid sources are known for the entire Peloponnese (e.g., Pe-Piper & Koukouvelas, 1990, 1992; Pe-Piper & Piper, 1991). The granitoid-bearing provenance of the conglomerate-dominated lobes is similar to the syn-rift Korfiotissa and Ano Pitsa formations (Figs 5a and b), whereas the provenance of the rest of the RDF depositional units matches the Mavro delta (Figs 5c and d). This near coincidence in the clast composition between the Mavro delta (Fig. 5d) and the deposits with a Phyllites-Quartzites provenance in the RDF (Fig. 5c) and the fact that the deposits in Kefalari and Kyllini deltas are clearly different, contrasts with the compositional patterns observed for the deposits in the Kyllini and Kefalari deltas (compare Figs 5c, d on the one hand and 5e on the other). Although the Kyllini and Kefalari delta deposits also contain lithologies derived from the Phyllites-Quartzites Unit, their composition is different enough to exclude them as important sources of the RDF in the Amphithea depocentre. The proportion of phyllites in the Kyllini deposits (Fig. 5e) is considerably smaller than in the case of the deposits with a Phyllites-Quartzites provenance in the RDF (Fig. 5c). Any contribution of clasts from the Kyllini deposits should significantly decrease the content in phyllite clasts in the RDF in a proportion that is not observed in the compositional data (Fig.

5). The proportion of limestones in both the Kyllini and Kefalari deposits (Fig. 5e) is higher than in the case of the deposits with a Phyllites-Quartzites provenance in the RDF (Fig. 5c). As limestones are one of the most resistant lithologies found in the clasts, contribution from these two deltas should increase the content of limestones in the RDF and that pattern is not observed (Fig. 5c). From the clast composition analysis illustrated in Fig. 5, it is evident that the main sediment source for the Amphithea depocentre originated in the rift shoulder to the south via the Mavro delta, ~15 km W of the study area, with minor sediment sources from local intrabasinal highs or from the northern margin of the rift.

Palaeotransport directions

The directional structures measured in the RDF (lobe axes, channel thalwegs, scours, current ripples, and trough-cross stratification) can be divided into the following three clusters: i) the conglomerate-dominated lobes, ii) all other units below the ~6° unconformity and iii) all other units above the ~6° unconformity (Fig. 6). The analysis shows a clear rearrangement of the transport direction from mainly transverse to the strike of the internal faults in the units below the ~6° unconformity (Fig. 6b) to subparallel to fault strike in the units above the unconformity (Fig. 6c). This pattern cannot, however, be discerned for the conglomerate-dominated lobes (Fig. 6a). The orientation of these lobe axes suggests in any case that their sources were located towards the northwest of the study area. This observation is compatible with the present-day distribution of older units of similar composition (i.e. units containing granitoid clasts and lacking phyllites and other metamorphic clasts; Figs 5a and b), and it is therefore suggested that the conglomerate-dominated lobes were sourced from local intrabasinal highs towards the Xylokastro horst area (Fig. 1), detached in origin from the sedimentary system fed by the Mavro delta (Fig. 5).

DEPOSITIONAL ELEMENTS

Based on rock body geometry, dimensions, internal architecture, grain size distribution and unit boundaries, the 16 stratigraphic units identified in this study (Fig. 3) can be grouped into six different types of depositional elements (Fig. 7): type A - mudstone-dominated sheets (1, 11 and 14); type B - conglomerate-dominated lobes (2, 4, 5, 6, 9, 12 and 15); type C - conglomerate channel belts and sandstone sheets (3); type D - sandstone channel belts (7); type E - sandstone-dominated broad shallow lobes (8) and type F - sandstone-dominated sheets with broad shallow channels (10, 13 and 16). Their description and analysis is based on the approach made by Talling *et al.* (2012) for subaqueous sediment density flows and is presented in the following sections.

Type A - Mudstone-dominated sheets (units 1, 11 and 14)

Mudstone-dominated units 1, 11 and 14 are composed of stacked individual mudstone-dominated sheets that range between 8 and 25 m in thickness and can be traced for more than 2.5 km (Figs 7a, 8a, b and 9). The proportion of sandstone beds in these sheets is generally between 18 to 27% of the thickness. The deposits are characterised by 1 to 7 cm thick mudstone beds intercalated with 1 to 2 cm thick siltstones and 3 to 24 cm thick very fine to lower medium sandstones (Figs 8a and 9b). Mudstones in the RDF predominantly composed of variable proportions of calcium carbonate and argillaceous clay, i.e. marlstones, however due to uncertainty in determining this proportion in the field, the grain-size equivalent term mudstone is used in this study. The mudstones are found as tabular laminated beds and the sandstones constitute massive or laminated tabular beds with normal grading, typically with asymmetrical rippled tops. Plant remains are frequently found as small broken fragments (1 to 7 mm) within the fine lamination or as well preserved stems and leaves at the base of the beds (Fig. 9c). Moderate to high bioturbation is common, mainly represented by non-ornamented single vertical tubes 1 to 2 cm long (Fig. 9d). Rare 4 to 14 m thick intervals enriched in sandstone beds (up to 36 to 44% sandstones) of sheet or lenticular geometry intercalate the mudstone sheets (Fig. 8b). These sandstone beds are up to 45 cm thick and the grain size reaches lower coarse sand grade. They are frequently normal-graded and can be either structureless or develop current ripples at the top. The thickest sandstone beds preserve accumulations of muddy intraclasts at the base or as thin lenses. Very rarely, conglomerate lenses containing pebbles and cobbles up to 8 cm and 10 to 30 cm intraclasts supported in a sandy matrix are found, reaching 50 cm in thickness (Fig. 9e). The sandstone enriched intervals found in Unit 1 can be traced laterally for several hundreds of meters towards the east until they link with units 3, 7, 8 or 10 in the channel system (Fig. 3). To the west, the proportion of sandstone beds decreases progressively and the intervals terminate in tapering wedge geometries that pinch out over ~100 m (Fig. 9f).

The predominance of mudstone in type A units together with their planar geometry at the km scale indicates a subaqueous low energy environment below storm-wave base and with very low gradients, such as a basin floor plain (e.g. Johnson *et al*., 2001; Sumner *et al*., 2012). The mudstone beds are interpreted to represent suspension fallout and deposition from turbulent mud clouds (cf. Talling *et al*., 2012), whereas the occurrence of relatively thin sandstone beds with traction structures such as lamination and ripples indicate deposition from turbiditic flows (e.g. Dasgupta, 2003; Talling *et al*., 2012). The plant remains reflect the overall subaerial source of the depositional system. The development of coarser and thicker-bedded sandstone-enriched intervals with accumulation of intraclasts is interpreted as the progradation of distal lobes over the basin floor plain (e.g. Hodgson *et al*., 2006; Prélat *et al*., 2009, 2013; Spychala *et al*., 2017). The fact that the sandstone-enriched intervals in Unit 1 physically link with units 3, 7, 8 or 10 in the channel system, together with their progressive reduction in sandstone content away from the channel system and the characteristic tapering geometry of their terminations (Fig. 9f), suggest that they represent in this particular case, the lateral fringes of the channel system over the basin floor plain, sharing the same characteristics described for channel levees in other settings (e.g. Posamentier & Kolla, 2003; Di Celma *et al*., 2011; Morris *et al*., 2014).

Type B - Conglomerate-dominated lobes (units 2, 4, 5, 6, 9, 12 and 15)

The conglomerate-dominated lobes have convex tops with a typical wavelength of 100 to 300 m (Figs 7b and 10a) and occur as isolated bodies intercalated in the mudstone-dominated units 1, 11 and 14 (Figs 2 and 3). The lobes range in thickness from 5 to 20 m and their lateral extent is 50 to 1500 m. They are conspicuously affected by syn-sedimentary internal deformational features such as normal faults and clastic intrusions that result in the development of highly irregular bases (Figs 7b, and 10b, d). Internally, lobes are composed of stacked tabular conglomerate beds 0.1 to 1.6 m thick, intercalated with 4 to 70 cm thick sandstone lenses (Figs 7b, 8c and 10c). The proportion of conglomerates in these deposits varies from 60 to 82%. Conglomerate clasts vary in size from 1 to 15 cm and are supported by a poorly to moderately sorted lower coarse sandstone matrix. The clast fabric of the conglomerates is variable, ranging from chaotically orientated to more or less aligned parallel to the bedding and defining the stratification. The base of the conglomerate beds tends to be irregular and non-erosive, however, infrequent cases of conglomerate lenses with erosive bases occur. The sandstone lenses are finely laminated, down-cutting into previous sandstone lenses or draping the topography of the conglomerates below. These sandstones are moderately to well sorted, fine to medium in grain size and grain-supported.

The particular clast composition (Figs 5 and 7b) of the conglomerate-dominated lobes together with their isolated occurrence within the Type A mudstone-dominated sheets suggests a different origin than all other units in the area, sourced from local intrabasinal highs to the basin floor plain (Figs 1 and 5). The regular alternation in the stacking of conglomerate and sandstone beds in the lobes represents energy fluctuations in the subaqueous sediment density flows. Conglomerates were deposited from non-cohesive flows with intermediate characteristics between frictional laminar-flows and semiplastic transitional flows (e.g. Sohn et. al., 1997; Sohn, 2000; Dasgupta, 2003). Sandstones on the other hand, were deposited under more turbulent fluid flow conditions by non-channelised traction currents (e.g. Sohn et. al., 1997; Dasgupta, 2003). The pervasive development of syn-sedimentary deformational structures throughout these deposits suggests their deposition over a soft unconsolidated substrate (i.e. type A units) that was subjected to dewatering by sediment loading.

Type C - Conglomerate channel belts and sandstone sheets (Unit 3)

This depositional element is found towards the base of the channel system and is more than 100 m thick (Figs 3 and 11). It consists of sand-rich intervals (80% sandstones and 20% mudstones) tens of meters thick, intercalated with conglomerate-dominated channel belts 5 to 20 m thick (Figs 7c and 11c). The proportion of conglomerates in the channel belts is ~62%. The conglomerates are either tabular beds 0.2 to 1.2 m thick with irregularly flat bases, or erosive lenses 1 to 3 m thick that incise up to 2 m into underlying deposits (Fig. 8d). These conglomerate bodies are grain- to matrix-supported and poorly sorted with diffuse horizontal stratification, usually extending laterally for 10 to 40 m (Figs 12a and b). Planar cross-stratification is also present in a few cases, mainly restricted to the conglomerate lenses. The average grain size varies from 0.5 to 3 cm, with maximum sizes between 4 and 12 cm. Sandstone and mudstone intraclasts are especially frequent in these bodies in the lower half of the channel belts and span from 2 to 30 cm in length (Fig. 12c). Lenses of laminated medium to coarse sandstones and granule-grade conglomerates are intercalated with the conglomerates in the channel belts.

External to the channel belts, 80% of the deposits are sandstones and 20% are mudstones (Fig. 7c). These overbank deposits consist mainly of 0.5 to 1.2 m thick sandstone lenses intercalated with intervals composed of laminated and rippled 0.05 to 0.4 m thick tabular sandstone beds and centimetre thick massive or laminated mudstone and siltstone (Fig. 8e). The sandstones in the thick lenses are fine to very coarse and variably poor to very well sorted (Fig. 12d). They are frequently laminated, rarely cross-laminated, and very often normal-graded with current ripples developed only at the top surface of the deposit (Fig. 8e). They contain intraclasts typically 2 to 5 cm, but can be up to 20 cm long, floating within the bed or concentrated at specific levels. The tabular beds in contrast, are composed of well to very well sorted very fine to lower medium sandstones, with rare isolated intraclasts smaller than 2 cm.

Unit 3 shows interaction between high-energy channelized and mid- to low-energy non-channelized traction currents (e.g. Sohn et. al., 1997; Dasgupta, 2003; Talling *et al.*, 2012). The alternating conglomerate-dominated and sandstone-dominated intervals are therefore interpreted as a subaqueous migrating conglomeratic channel belt with finer-grained overbank deposits (e.g. Clark & Pickering, 1996; Posamentier & Kolla, 2003; Janocko *et al.*, 2013). The internal geometry of the channel belts, together with the presence of sandstone lenses between the conglomerate bodies, show that the channel belts were filled by multiple depositional events from subaqueous sediment density flows of variable energy. The deposition of a dominantly conglomerate fraction in the channel belts is interpreted as an evidence for bypassing of the finer-grained fractions of sediment down-system (e.g. Hubbard *et al.*, 2014; Stevenson *et al.*, 2015; Li *et al.*, 2016). The concentration of sandstone and mudstone intraclasts towards the lower half of the channel belts reflects erosion of the overbank deposits during initial excavation of the channel belt.

Type D - Sandstone channel belts (Unit 7)

Unit 7 is the second depositional unit in the channel system and is characterized by the development of a 17 m thick channel belt towards the top of the unit that extends laterally for more than 300 m (Figs 3, 7d, 11a, b and 11d). The channel belt deposits are predominantly composed by sandstones (81%), with a smaller contribution of mudstones (9 to 16 %), conglomerates (up to 2.5%) and intraclast conglomerates (up to 8%). In contrast, the overbank deposits have a smaller representation of sandstones (64%) and higher proportion of mudstones (29%) with intraclast conglomerates in some cases (up to 7%). Individual channel elements in the belt are up to 12 m thick and 140 m wide. The channel fill is composed of very broad sandstone lenses 0.3 to 1.4 m thick, intercalated with up to 50 cm thick intervals of mudstones and tabular rippled and laminated well sorted very fine to medium sandstones and siltstones (Fig. 8f). The stratal geometry within each channel defines large scale low angle trough cross stratification, given by the gradual thickening of the sandstone lenses towards the middle of the troughs and thinning away until pinching out against the margins of the channels (Fig. 11d). The sandstone lenses are also observed to onlap onto the top of the channel banks once the channel depressions become filled. Intraclast conglomerates (Figs 8f, 12e, f) are found both as flat-lying lenses at the base of the channels and as wedges accreted to the lateral margins of the channel (Fig. 11d). These lateral wedges onlap the channel margins and downlap progressively and asymptotically onto the channel base away from the margins, thinning towards the thalweg of the channel (Fig. 11d). Channelization does not appear to follow any particular vertical pattern. The different scales of channelization observed (lenses, troughs and channel elements) within the channel belts are evenly distributed laterally giving way to the development of multiple internal erosional surfaces. The broad sandstone lenses are planar or cross laminated, well sorted and medium to coarse-grained, with intraclasts 1 to 15 cm long, floating or aligned along the stratification. Pebble lags are common at the base of the channel elements. The deposits external to the channel belt are composed mostly of well sorted fine to very fine tabular sandstone beds, 5 to 40 cm thick, with planar lamination and ripples at the top. These sandstone beds are interbedded with centimetre-thick structureless or laminated mudstones and rippled siltstones and very fine sandstones (Figs 8g and 12g).

This channel belt resulted from the migration and erosion of a series of trunk channels through overbank deposits in a subaqueous environment dominated by sediment density flows (e.g. Clark & Pickering, 1996; Posamentier & Kolla, 2003; Janocko *et al.*, 2013). Deposition inside and outside the channels was essentially similar, consisting of episodic deposition of sand by traction currents separated by thin mudstones denoting pauses and suspension fallout (e.g. Dasgupta, 2003; Talling *et al.*, 2012). The overall coarser size of the sandstones in the channel fill (Fig. 8f) indicates that deposition in the channels occurred at higher energy levels than those recorded by the overbank deposits (Fig. 8g). Similarly, the presence of lithic pebble lags in the channels (Fig. 8f) suggests that the processes responsible for the channel cuttings were more energetic than those that led to the filling of these erosive features with predominantly sandstone deposits. The composite nature of the channel belt together with the pebble lag deposits and wedges of intraclast conglomerates at the base and margins of the channel elements indicate bypassing of sediment down-system (e.g. Hubbard *et al.*, 2014; Stevenson *et al.*, 2015; Li *et al.*, 2016). Similarly, the alternation of thick sandstone lenses and thinner-bedded and finer-grained intervals that characterise the channel fill indicates the existence of multiple discrete depositional events during the lifetime of each channel element (e.g. Hubbard *et al.*, 2014; Stevenson *et al.*, 2015; Li *et al.*, 2016). The wedges of intraclast conglomerates in the overbank deposits (Fig. 8g) are interpreted to originate from the burst and collapse of the channel levees and deposition of crevasse-splays.

Type E - Sandstone-dominated broad shallow lobes (Unit 8)

This unit is sandstone-dominated (94%) with a minor amount of conglomerates (5%) and mudstones (1%) (Fig. 7e). It is characterised by the development of thick lensoidal beds (60 to 140 cm thick) of moderately sorted medium to very coarse sandstones that are continuous for hundreds of meters (Figs 11a, b and d). The base of these lenses can be locally highly erosive, but also extending flatly for tens of meters. Although there is a tendency for the tops to be generally flat, it is not uncommon to found lenses with gently convex tops. The conglomerates have grains 1 to 3 cm long supported in a moderately sorted medium sandstone matrix. They constitute 0.3 to 1 m thick bodies transitional at the base of the sandstone beds or also found as individual erosive lenses (Fig. 8h). The stacking of sandstone and conglomerate lenses defines, in some places, lobate bodies with distinctive convex tops that taper laterally from 4 m to 1 m thick over a horizontal distance in the order of 50 m (Fig. 8h). Due to the variable nature of the bases of the sandstone and conglomerate bodies the lobes also can develop erosive bases (Fig. 12h). Finer-grained deposits such as mudstones and very fine to fine rippled sandstones appear intercalated between the thick sandstone and conglomerate lenses in intervals less than 30 cm thick (Fig. 12i).

The characteristic rock-body geometry of Unit 8 together with the predominance of thick bedded sandstone beds are typical features of subaqueous sediment density flow lobe complexes, consisting of stacked and partially amalgamated lobe elements (e.g. Prélat *et al*., 2009, 2013). Thick sandstone beds are interpreted to have been deposited by progressive aggradation from high-density sediment flows (e.g. Kneller & Branney., 1995; Talling *et al*., 2012). The erosive nature of the basal boundaries of some sandstone beds, conglomerate lenses and lobe elements indicates sediment bypassing (e.g. Stevenson *et al*., 2015), which is often associated to a proximal position in the lobe setting, close to the channel-lobe transition (e.g. Normark *et al*., 1979; Wynn *et al*., 2002; Pemberton *et al*., 2016; Brooks *et al*., 2018).

Type F - Sandstone-dominated sheets with broad shallow channels (units 10, 13 and 16)

These units are exposed as sandstone-dominated sheets 30 to 65 m thick, extending laterally for more than 3.5 km (Fig. 7f). Type F units are found at the top of the channel system (Unit 10) or above the ~6° unconformity (units 13 and 16) intercalated with Type A mudstone-dominated units 11 and 14 (Figs 3, 11a, b, f and 13a). Sandstone content ranges from 63 to 87% with conglomerates accounting for 16 to 25% and mudstones representing 9 to 19% of the thickness of the sheets. The deposits are mostly composed of laterally elongated sandstone channels (46 to 66%), 0.3 to 4 m thick and up to 70 m wide (Fig. 13c). Their grain size varies from medium to very coarse sand, typically containing floating mudstone and sandstone intraclasts 1 to 13 cm in length that can reach maximum sizes of 26 to 50 cm (Fig. 8i). The sandstone channels are diffusely laminated or stratified with sharp erosive concave to subplanar bases. Conglomerates are usually found at the base of the sandstone channel bodies as amalgamated laminated and stratified grain-supported moderately to well sorted lenses (Fig.

13d). More rarely, the conglomerates occur as isolated tabular beds 0.5 to 2 m thick in which clasts are supported by a fine to coarse sandstone matrix. Grain size varies from 0.2 to 5 cm in average and maximum of 15 cm. Mudstone and sandstone intraclasts are also present in the conglomerate bodies. The sandstone and conglomerate bodies intercalate 0.2 to 1.2 m thick intervals of centimetric tabular beds of mudstones and rippled siltstones and very fine to medium sandstones (Fig. 13b). Tabular bodies, 1 to 3 m thick, composed of intensively sheared and folded mudstone and sandstone intraclasts also occur in the deposits corresponding to Unit 13. Intraclasts are up to 150 cm long and supported in a chaotic mudstone-rich matrix with occasional floating granules and pebbles. The orientation of the intraclasts is generally random and only the largest and most elongated tend to align subparallel to the bedding (Fig. 13e).

The great lateral extent of Type F units, their sheet geometry and the abundance of broad shallow channels allow for its interpretation as a subaqueous sediment density flow distributary fan setting (e.g. Posamentier & Kolla, 2003; Hodgson *et al*., 2006; Oluboyo *et al*., 2014). The geometry of the channels and their deposits indicate shallow erosion by traction currents and bypassing of sediment down-system before being filled by progressive aggradation from high-density sediment flows (e.g. Kneller & Branney, 1995; Talling *et al*., 2012). The rippled thin-bedded sandstones and siltstones in the overbank intervals are interpreted as deposits from unconfined turbulent flows, low-density turbidity currents (e.g. Dasgupta, 2003; Talling *et al*., 2012), whereas the mudstones represent deposition from suspension fallout (e.g. Dasgupta, 2003; Talling *et al*., 2012). The intraclast conglomerates among the overbank intervals are interpreted as debris flow deposits (e.g. Sohn *et al*., 1997; Sohn, 2000; Dasgupta, 2003) that originated from the gravitational instability of unconsolidated deposits, as is demonstrated by the soft-sediment deformational features observed in the intraclasts.

SLIDE SHEETS

The stratigraphically youngest RDF exposures in the northern part of the Amphithea fault block show a succession of slide sheets stacked in a complex that exceeds 200 m of thickness (Figs 2a, b, 3 and 14). Dip sections of the slide sheets are well exposed along vertical cliffs on the margins of the SE to NE orientated drainage network (Fig. 2a), but strike sections are not so well developed and tend to be covered in vegetation. Only the frontal and posterior ends of the slide sheets are thus exposed and no lateral terminations or structures such as tear faults can be observed. The individual slide sheets contain mainly portions of Unit 16, thrusted along slices of Unit 14, ranging in thickness from 10 to 30 m (occasionally up to 70 m) and dipping more steeply than the units in the RDF exposed immediately to the south (Fig. 2a, b). Mapping of the individual slide sheets is limited by the extent of the outcrops, ranging from 200 to more than 500 m in both dip and strike direction. Thrust ramp and flat geometries can be identified and strike predominantly northwest-southeast (Fig. 14c) and have a northeast sense of vergence (Fig. 14d). This strike orientation is parallel to that of the north and south boundary fault systems of the Amphithea fault block and is oblique to internal normal faults (Figs 1, 2a, b and 14e).

Subaqueous translational and rotational slides (or slumps) happen in a wide range of slopes, from as shallow as <1° to very steep scarps (e.g. Lewis, 1971; Bull *et al*., 2009; Moernaut & de Batist, 2011). The occurrence of thrusted slide sheets tend to develop towards the lower reaches of the slope (toes), where the slides arrest (e.g. Lewis, 1971; Frey Martinez *et al*., 2005, 2006; Bull *et al*., 2009; Moernaut & de Batist, 2011). The fact that the slide complex exceeds 200 m in thickness implies at least a similar throw in the northern boundary fault system in order to accommodate such a stacking of slide sheets. This magnitude of fault throw could not be achieved without the consequent tilting of the Amphithea hangingwall towards the NNE. The slide sheets are thus interpreted to have originated as a result of the tilting of the hangingwall block towards the NNE after deposition of Unit 16 (Figs 2a, b, 3 and 14). The strong lithological contrast between mudstone-dominated Unit 14 and sandstone-dominated Unit 16 encouraged development of detachments towards the upper part of Unit 14 (Fig. 14f). These detachments allowed slices of units 14 and 16 to slide, following the hangingwall palaeoslope towards the northeast, stacking one on top of the other against the northern margin of the Amphithea fault block (Fig. 14g). It is unclear however, whether the triggering and downslope slide of these sheets occurred as one major subaqueous landslide or rather as a series of gravitational instability events spaced through time. Similarly, the relative duration of the landslide/s cannot be constrained. Presence of tight sheath folding and *boudinage* at basal detachment zones in slides is often attributed to creep (e.g. Lucente & Pini, 2003). None of these structures are observed for the present case; however, the sharp thrusts developed instead, may reflect mainly the contrasting competence of the lithologies involved with no implications for the duration of the slides.

DISCUSSION

Sedimentary and tectonic evolution of the Rethi-Dendro Formation in the Amphithea fault block

The sedimentary analysis of the depositional elements and the different stratigraphic units allows a better understanding of the evolution of the lacustrine deep-water environment of the RDF. In particular, the recognition of angular unconformities within the stratigraphic units is used to identify major phases of hangingwall tilting and their control on the subaqueous environments (e.g., Ravnås & Steel, 1997; Muravchik *et al*., 2017). The clast composition of the RDF in the Amphithea fault block remains unchanged during its evolution, indicating more-or-less fixed sediment sources. However, large changes in palaeotransport direction are observed across the ~6° unconformity which are analysed below in terms of the structural configuration of the Amphithea fault block and its tectonic context in the Corinth Rift. The link between the sedimentary evolution of the RDF to changes in lake/marine level or climate is difficult to constrain, but possible scenarios are discussed.

Deposition below the ~6° angular unconformity

Below the ~6° angular unconformity (Fig. 15a, b, c), the Amphithea fault block had a halfgraben configuration defined by the Koutsa and Melissi faults towards the northwest and north and the

Amphithea fault at the southern margin (Gawthorpe *et al.*, 2017b). The RDF was characterised by a mudstone-dominated succession (Unit 1) and a channel system (units 3, 7, 8 and 10) sourced from the Mavro delta and conglomerate-dominated lobes derived from the Xylokastro high (units 2, 4, 5, 6, 9). The channel system displays an overall change in depositional style from channel complexes in the lower half (units 3 and 7) to lobe complexes in the upper half (units 8 and 10), denoting a clear retrogradational pattern. Similarly, the coarser grain-sizes are mainly concentrated in the basal Unit 3. Although conglomerates are sparsely developed throughout all the channel system units, it is only in Unit 3 that conglomerate beds are fully developed and clast sizes reach dimensions comparable to those found in the Mavro delta (Rohais *et al.*, 2007). Retrogradation of deep-water channel systems is a typical processes that can be ascribed to autocyclicity of the depositional system or due to variations in the base level (sea/lake) (e.g. Normark *et al.*, 1979; Wynn *et al.*, 2002; Posamentier & Kolla, 2003; Pemberton *et al.*, 2016; Brooks *et al.*, 2018). In this particular case, its exact origin cannot be established from the data collected. No clear indication of tectonic controls in the Amphithea fault block on this retrogradation have been found, apart from the ~8° angular unconformity immediately below the channel system exposures in Fault Block 1. However, the reduced level of exposure of this structure prevents any attempt of linking its presence with the evolution of the channel system.

The tilting of the hangingwall was towards the northeast, whereas the orientation of the channel system was NW-SE with flow towards the southeast, parallel to the fault-controlled margins of the Amphithea fault block and perpendicular to the internal faults in the depocentre (Figs 6b, 15a). The channel system is interpreted to have been diverted to the southeast by the down-stepping internal faults, once it emerged from the constriction between the Amphithea and Xylokastro highs and entered the Amphithea hangingwall block (Fig. 15a). The thickest channel system deposits (at Riza hill) lie in close proximity to the axis of the synformal monocline flexure that runs parallel to and in the hangingwall of the Amphithea fault (Fig. 2a). This present-day flexure originated in front of a steepening monocline limb developed above the growing, but blind Amphithea fault (Figs 4a, b, c and 15a, b, c). The location and orientation of the channel system is thus interpreted to have been controlled by the position of these coupled positive and negative topographic features (e.g. Kane *et al.*, 2010) in conjunction with the gradients caused by the internal faults.

Development of the ~6° angular unconformity

The ~6° angular unconformity results from the tilting of the Amphithea hangingwall towards the NNE as a result of displacement on the S-dipping Melissi fault along the northern margin of the depocentre (Fig. 15b). Such magnitude of tilting implies a throw of at least 500 m on the northern boundary system for a halfgraben with the dimensions of the Amphithea fault block. This generated enough accommodation that mudstone became the dominant sediment accumulating in the hangingwall (Unit 11, Fig. 15b). The channel system as a whole, is interpreted to have migrated closer to the northern boundary fault system due to ground tilting (e.g. Kane *et al.*, 2010). However, this hypothesis cannot be tested because only higher levels of the stratigraphy are currently exposed.

Deposition above the ~6° angular unconformity

The stratigraphy above the ~6° angular unconformity alternates between mudstone-dominated sheets (units 11 and 14; Figs 15b and 15d) and sandstone-dominated sheets with broad shallow channels (units 13 and 16; Figs 15c and 15e), with intercalations of conglomerate-dominated lobes sourced from the Xylokastro high (units 12 and 15; Figs 15c and 15d). Palaeotransport directions measured in deposits sourced from the Mavro delta (units 11, 13, 14 and 16) are predominantly towards the northeast, orientated subparallel to the internal faults within the Amphithea hangingwall (Fig. 6c). This is interpreted to reflect the persistence throughout these stratigraphic units of a basin floor topographic gradient towards the S-dipping fault boundary (Melissi fault) in the northern margin of the Amphithea fault block. However, the conformable nature of units above the ~6° angular unconformity indicates that the changes in the depositional system (alternating mudstone and sandstone-dominated units) are not directly related to hangingwall tilting events in the Amphithea hangingwall that could have re-routed the supply of sediment away from this sector of the basin. This alternation was probably controlled by processes external to the depositional setting: e.g. tectonics in the source area, climatic modulation, variations in base level of the water body (lake/sea) or autocyclicity of the deltaic feeder system. The Mavro delta is interpreted to have a dominant northwards progradation direction and radial distribution of palaeocurrents (Rohais *et al.*, 2007), so its sourcing to the Amphithea fault block could have been subjected to autocyclic shifting of the delta lobes, leading to periods of reduced delivery of sand and coarser sediment to the depocentre and development of the thick accumulations of mudstone-dominated units 11 and 14.

Large scale subaqueous landslide

The thick succession of slide sheets found at the top of the RDF in the area (Figs 2a, b, and 14) represents the end of the Amphithea hangingwall as an effective sediment fairway to deeper and more distal regions in the basin to the east (Fig. 15f). The triggering of this large scale subaqueous slide complex is interpreted to be due to tectonic activity on the faults bounding the southern and northern margin of the Amphithea fault block and associated to the tilting of the hangingwall towards the NNE. The fact that the slide complex is overlain by the Pleistocene Kryoneri delta and marine terraces indicates that uplift of the Amphithea fault block ensued after the emplacement of the slide sheets (Gawthorpe *et al.*, 2017a, 2017b). However, it is highly probable that the tilting of the Amphithea hangingwall and triggering of the slide sheets represent an early manifestation of this uplifting process.

Structural controls on basin-floor gradients

Changes in bathymetry due to evolving structures are known to affect the deposition of deep-water sedimentary systems (e.g. Haughton, 2000; Hodgson & Haughton, 2004; Gee & Gawthorpe, 2006; Kane *et al.*, 2010; Oluboyo *et al.*, 2014; Ge *et al.*, 2017, 2018; Maier *et al.*, 2017, 2018). In this study, the subaqueous flows derived from the Mavro delta followed regional, basin-scale, gradients and in their path along the Amphithea fault block were forced to interact with more local structural features such as the presence of internal faults, a tilted hangingwall and monocline flexures on top of growing faults, which in turn, affected their transport and deposition. The RDF in the Amphithea fault block records the interplay between two different fault orientations (Figs 1 and 2a): NE-SW striking faults (internal faults and Koutsa border fault) and NW-SE striking faults (Amphithea and Melissi border faults). Faults of both orientations were active throughout the deposition of the RDF in the study area. Nevertheless, the NE-SW striking faults had a defining control on the orientation of the Mavro derived sedimentary system below the ~6° angular unconformity, while the NW-SE striking faults become the predominant ones after the generation of the ~6° angular unconformity, as observed from the reorientation of the palaeotransport directions across this unconformity (Figs 6b, c and 15).

Intrabasinal highs

The presence of the Xylokastro and Amphithea intrabasinal highs played a fundamental role in funnelling the subaqueous flows from the Mavro delta into the Amphithea hangingwall as well as sourcing the conglomerate-dominated lobes (units 2, 4, 5, 6, 9, 12 and 15). In the case of the Amphithea high it also functioned as a barrier from material sourced from the south, as the compositional analysis of the RDF shows lack of the low grade metamorphic clasts that characterise the Kefalari delta located along the southern margin of the fault block south of the Amphithea high (Figs 1 and 5).

Fault block uplift

Sediment fairways in rift basins have a limited lifetime due to the dynamics of the fault networks that define them. Processes such as fault block uplift and subsidence and migration of fault activity are thus responsible for changes in the physiography of the basin, leading to new sediment transport pathways and destruction or enhancement of previous ones (e.g., Leeder & Gawthorpe, 1987; Ravnås & Steel, 1998; Gawthorpe & Leeder, 2000). The Amphithea fault block is an example of a depocentre that evolved from being an effective transport pathway for sediment sourced from the Mavro delta to being an area dominated by gravitational sliding from its southern margin due to fault activity. Ultimately, uplift of the Amphithea fault block occurred, signalling its demise as a depocentre and leading to its subaerial exposure and incision (Gawthorpe *et al.*, 2017a, 2017b). The passage from subsidence to uplift in the area reflects the northward migration of the fault activity and concurrent uplift of the southern fault blocks that is observed throughout the Corinth Rift (e.g. Bentham *et al.*, 1991; Leeder *et al*., 2005; Rohais *et al*., 2007; Ford *et al*., 2013; Gawthorpe *et al*., 2017b). During deposition of most of the RDF in the Amphithea fault block the coastline was situated towards the southern margin of the basin, forming a large embayment from the Kefalari and Trikala faults towards the Mavro delta (Figs 1 and 15; Gawthorpe *et al*., 2017b). As faulting migrated northwards, the activity of the Amphithea fault increased, leading to further uplift of the Amphithea high, renewed tilting of the Amphithea hangingwall and triggering of large scale gravitational sliding in the depocentre. Further migration of fault activity shifted the subsiding areas towards the present day Gulf of Corinth and uplifted southern fault blocks such as the Amphithea depocentre (e.g. Rohais *et al*., 2007; Ford *et al*., 2013; Gawthorpe *et al*., 2017b). This processes of fault migration and uplift of the fault blocks in rift basins may lead to the complete erosion of the most proximal early syn-rift successions in more mature basins such as the Red Sea, North Sea and the Atlantic margin (e.g. Steckler *et al*., 1988; Nøttvedt *et al*., 2000; Ravnås *et al*., 2000; Bosworth *et al*., 2005; Torsvik *et al*., 2009; Moulin *et al*., 2010). Hence, the implications of the present study provide important insights into the evolution of early syn-rift deep-water successions that are seldom preserved on the rift shoulders.

CONCLUSIONS

- Different stages of hangingwall tilt at both large- and local scale and the interaction between them are primary controls on the evolution of the deep-water environment in rift basins, determining the orientation of the depositional systems, their depositional style and stacking patterns.
- Studies of clast composition coupled with the analysis of palaeotransport directions are fundamental for a correct assessment of the subaqueous drainage patterns, especially in the recognition of transverse and axial drainage and identification of different sediment sources.
- The RDF in the Amphithea fault block represents deposition of a subaqueous, deep-water axial transport system sourced from the Mavro delta and, to a much smaller degree, by local intrabasinal sources (Xylokastro and Amphithea highs).
- Deformation of the hangingwall determined changes in the orientation of the depositional systems due to a combination of the large scale tilt of the fault block by its border faults and the activity of the smaller faults internal to the depocentre.
- The structural evolution of the Amphithea faut block shows the interaction between active structures of two different orientations: NE-SW (internal faults and Koutsa border fault) and NW-SE (Amphithea and Melissi border faults).
- The end of the Amphithea fault block as a deep-water depocentre is marked by the development of large-scale sliding originated from the steepening of its tilted hangingwall and it is interpreted to represent an early symptom of fault block uplift in the area.

Our findings have implications for deep-water rift basin studies in general. The existence of two or more fault orientations influencing the hangingwall gradients is a problem usually tackled from a structural geology perspective (e.g. Morley *et al.*, 2004; Henza *et al.*, 2010, 2011), and ignored in most sedimentary models for deep-water environments (e.g. Ravnås & Steel, 1997; Gawthorpe & Leeder, 2000; Leppard & Gawthorpe, 2006; Zhang & Scholz, 2015; Henstra *et al.*, 2016). This aspect needs better documentation in order to understand the timing of deformation and its control on deep-water systems. Correct identification and mapping of intrabasinal highs is also crucial in attributing different sediment sources and barriers to axial and transverse subaqueous drainage in rift basins.

ACKNOWLEDGMENTS

This contribution forms part of the Syn-Rift Systems Project funded by the Research Council of Norway, Aker BP, ConocoPhillips, DNO, Equinor, Neptune and Tullow Oil (project number 255229) to the University of Bergen and academic partners the universities of Leeds, East Anglia, Lorraine and the National and Kapodistrian University of Athens. The authors' thank the Segas family for help and support whilst undertaking fieldwork in the Corinth rift. Reviews by Oliver B. Duffy, Jonathan Obrist-Farner, Benzhong Xian and an anonymous reviewer and editorial steering by Cari Johnson are acknowledged. The authors have no conflict of interest to declare.

REFERENCES

ARMITAGE, D.A., MCHARGUE, T., FILDANI, A. & GRAHAM, S.A. (2012) Postavulsion Channel Evolution: Niger Delta Continental Slope. *AAPG Bulletin*, **96,** 823-843.

AZPIROZ-ZABALA, M., CARTIGNY, M.J.B., TALLING, P.J., PARSONS, D.R., SUMNER, E.J., CLARE, M.A., SIMMONS, S.M., COOPER, C. & POPE, E.L. (2017) Newly Recognized Turbidity Current Structure Can Explain Prolonged Flushing of Submarine Canyons. *Science Advances*, **3,** e1700200.

BENTHAM, P., COLLIER, R.E.L., GAWTHORPE, R.L., LEEDER, M.R., PROSSOR, S. & STARK, C. (1991) Tectono-Sedimentary Development of an Extensional Basin: The Neogene Megara Basin, Greece. *Journal of the Geological Society*, **148,** 923-934.

BORNOVAS, J., LALECHOS, N., FILIPPAKIS, N., CHRISTODOULOU, G. & TSAILA-MONOPOLI, S. (1972) Geological map of Greece: 1:50,000, Nemea Sheet. IGME Publications, Athens, Greece.

BOSWORTH, W., HUCHON, P. & MCCLAY, K.R. (2005) The Red Sea and Gulf of Aden Basins. *Journal of African Earth Sciences*, **43,** 334-378.

BROOKS, H.L., HODGSON, D.M., BRUNT, R.L., PEAKALL, J., HOFSTRA, M. & FLINT, S.S. (2018) Deep-Water Channel-Lobe Transition Zone Dynamics: Processes and Depositional

Architecture, an Example from the Karoo Basin, South Africa. *Geological Society of America Bulletin*, **130,** 1723-1746.

BULL, S., CARTWRIGHT, J. & HUUSE, M. (2009) A Review of Kinematic Indicators from Mass-Transport Complexes Using 3d Seismic Data. *Marine and Petroleum Geology*, **26,** 1132-1151.

CARVAJAL, C., PAULL, C.K., CARESS, D.W., FILDANI, A., LUNDSTEN, E., ANDERSON, K., MAIER, K.L., MCGANN, M., GWIAZDA, R. & HERGUERA, J.C. (2017) Unraveling the Channel–Lobe Transition Zone with High-Resolution AUV Bathymetry: Navy Fan, Offshore Baja California, Mexico. *Journal of Sedimentary Research*, **87,** 1049-1059.

CLARK, J.D. & PICKERING, K.T. (1996) Architectural Elements and Growth Patterns of Submarine Channels: Application to Hydrocarbon Exploration. *AAPG Bulletin*, **80,** 194-221.

COLLIER, R.E.L. & DART, C.J. (1991) Neogene to Quaternary Rifting, Sedimentation and Uplift in the Corinth Basin, Greece. *Journal of the Geological Society, London*, **148,** 1049-1065.

COWIE, P.A., GUPTA, S. & DAWERS, N.H. (2000) Implications of Fault Array Evolution for Synrift Depocentre Development: Insights from a Numerical Fault Growth Model. *Basin Research*, **12,** 241-261.

DASGUPTA, P. (2003) Sediment Gravity Flow - the Conceptual Problems. *Earth-Science Reviews*, **62,** 265-281.

DEPTUCK, M.E., SYLVESTER, Z., PIRMEZ, C. & O'BYRNE, C. (2007) Migration–Aggradation History and 3-D Seismic Geomorphology of Submarine Channels in the Pleistocene Benin-Major Canyon, Western Niger Delta Slope. *Marine and Petroleum Geology*, **24,** 406-433.

DI CELMA, C.N., BRUNT, R.L., HODGSON, D.M., FLINT, S.S. & KAVANAGH, J.P. (2011) Spatial and Temporal Evolution of a Permian Submarine Slope Channel-Levee System, Karoo Basin, South Africa. *Journal of Sedimentary Research*, **81,** 579-599.

FABUEL-PÉREZ, I., HODGETTS, D. & REDFERN, J. (2009) A New Approach for Outcrop Characterization and Geostatistical Analysis of a Low-Sinuosity Fluvial-Dominated Succession Using Digital Outcrop Models: Upper Triassic Oukaimeden Sandstone Formation, Central High Atlas, Morocco. *AAPG Bulletin*, **93,** 795-827.

FERENTINOS, G., PAPATHEODOROU, G. & COLLINS, M.B. (1988) Sediment Transport Processes on an Active Submarine Fault Escarpment: Gulf of Corinth, Greece. *Marine Geology*, **83,** 43-61.

FILDANI, A., HUBBARD, S.M., COVAULT, J.A., MAIER, K.L., ROMANS, B.W., TRAER, M. & ROWLAND, J.C. (2013) Erosion at Inception of Deep-Sea Channels. *Marine and Petroleum Geology*, **41,** 48-61.

FORD, M., ROHAIS, S., WILLIAMS, E.A., BOURLANGE, S., JOUSSELIN, D., BACKERT, N. & MALARTRE, F. (2013) Tectono-Sedimentary Evolution of the Western Corinth Rift (Central Greece). *Basin Research*, **25,** 3-25.

FREY MARTINEZ, J., CARTWRIGHT, J. & HALL, B. (2005) 3d Seismic Interpretation of Slump Complexes: Examples from the Continental Margin of Israel. *Basin Research*, **17,** 83-108.

FREY-MARTÍNEZ, J., CARTWRIGHT, J. & JAMES, D. (2006) Frontally Confined Versus Frontally Emergent Submarine Landslides: A 3d Seismic Characterisation. *Marine and Petroleum Geology*, **23,** 585-604.

GAWTHORPE, R.L. & LEEDER, M.R. (2000) Tectono-Sedimentary Evolution of Active Extensional Basins. *Basin Research*, **12,** 195-218.

GAWTHORPE, R.L., ANDREWS, J.E., COLLIER, R.E.L., FORD, M., HENSTRA, G.A., KRANIS, H., LEEDER, M.R., MURAVCHIK, M. & SKOURTSOS, E. (2017a) Building up or Out? Disparate Sequence Architectures Along an Active Rift Margin—Corinth Rift, Greece. *Geology*, **45,** 1111-1114.

GAWTHORPE, R.L., LEEDER, M.R., KRANIS, H., SKOURTSOS, E., ANDREWS, J.E., HENSTRA, G.A., MACK, G.H., MURAVCHIK, M., TURNER, J.A. & STAMATAKIS, M. (2017b) Tectono-Sedimentary Evolution of the Plio-Pleistocene Corinth Rift, Greece. *Basin Research*. 10.1111/bre.12260.

GE, Z., NEMEC, W., GAWTHORPE, R.L. & HANSEN, E.W.M. (2017) Response of Unconfined Turbidity Current to Normal-Fault Topography. *Sedimentology*, **64,** 932-959.

GE, Z., NEMEC, W., GAWTHORPE, R.L., ROTEVATN, A. & HANSEN, E.W.M. (2018) Response of Unconfined Turbidity Current to Relay-Ramp Topography: Insights from Process-Based Numerical Modelling. *Basin Research*, **30,** 321-343.

GEE, M.J.R. & GAWTHORPE, R.L. (2006) Submarine Channels Controlled by Salt Tectonics: Examples from 3d Seismic Data Offshore Angola. *Marine and Petroleum Geology*, **23,** 443-458.

GEE, M.J.R., GAWTHORPE, R.L., BAKKE, K. & FRIEDMANN, S.J. (2007) Seismic Geomorphology and Evolution of Submarine Channels from the Angolan Continental Margin. *Journal of Sedimentary Research*, **77,** 433-446.

HAUGHTON, P.D.W. (2000) Evolving Turbidite Systems on a Deforming Basin Floor, Tabernas, Se Spain. *Sedimentology*, **47,** 497-518.

HENSTRA, G.A., GRUNDVÅG, S.-A., JOHANNESSEN, E.P., KRISTENSEN, T.B., MIDTKANDAL, I., NYSTUEN, J.P., ROTEVATN, A., SURLYK, F., SÆTHER, T. & WINDELSTAD, J. (2016) Depositional Processes and Stratigraphic Architecture within a Coarse-Grained Rift-Margin Turbidite System: The Wollaston Forland Group, East Greenland. *Marine and Petroleum Geology*, **76,** 187-209.

HENZA, A.A., WITHJACK, M.O. & SCHLISCHE, R.W. (2010) Normal-Fault Development During Two Phases of Non-Coaxial Extension: An Experimental Study. *Journal of Structural Geology*, **32,** 1656-1667.

HENZA, A.A., WITHJACK, M.O. & SCHLISCHE, R.W. (2011) How Do the Properties of a Pre-Existing Normal-Fault Population Influence Fault Development During a Subsequent Phase of Extension? *Journal of Structural Geology*, **33,** 1312-1324.

HODGETTS, D. (2009) LiDAR in the environmental sciences: geological applications. In: *Laser Scanning for the Environmental Sciences* (Ed. by G. Heritage, A. Large), pp. 165–179. Wiley-Blackwell, Oxford.

HODGSON, D.M. & HAUGHTON, P.D.W. (2004) Impact of Syndepositional Faulting on Gravity Current Behaviour and Deep-Water Stratigraphy: Tabernas-Sorbas Basin, Se Spain. In: *Confined Turbidite Systems* (Ed. by Lomas S. A. & Joseph P.) *Geological Society, London, Special Publications*, **222,** 135-158.

HODGSON, D.M., FLINT, S.S., HODGETTS, D., DRINKWATER, N.J., JOHANNESSEN, E.P. & LUTHI, S.M. (2006) Stratigraphic Evolution of Fine-Grained Submarine Fan Systems, Tanqua Depocenter, Karoo Basin, South Africa. *Journal of Sedimentary Research*, **76,** 20-40.

HUBBARD, S.M., ROMANS, B.W. & GRAHAM, S.A. (2008) Deep-Water Foreland Basin Deposits of the Cerro Toro Formation, Magallanes Basin, Chile: Architectural Elements of a Sinuous Basin Axial Channel Belt. *Sedimentology*, **55,** 1333-1359.

HUBBARD, S.M., COVAULT, J.A., FILDANI, A. & ROMANS, B.W. (2014) Sediment Transfer and Deposition in Slope Channels: Deciphering the Record of Enigmatic Deep-Sea Processes from Outcrop. *Geological Society of America Bulletin*, **126,** 857-871.

JACKSON, C.A.L., LARSEN, E., HANSLIEN, S. & TJEMSLAND, A.E. (2011) Controls on Synrift Turbidite Deposition on the Hanging Wall of the South Viking Graben, North Sea Rift System, Offshore Norway. *AAPG Bulletin*, **95,** 1557-1587.

JANOCKO, M., NEMEC, W., HENRIKSEN, S. & WARCHOŁ, M. (2013) The Diversity of Deep-Water Sinuous Channel Belts and Slope Valley-Fill Complexes. *Marine and Petroleum Geology*, **41,** 7-34.

JOHNSON, S.D., FLINT, S.S., HINDS, D. & DE VILLE WICKENS, H. (2001) Anatomy, Geometry and Sequence Stratigraphy of Basin Floor to Slope Turbidite Systems, Tanqua Karoo, South Africa. *Sedimentology*, **48,** 987-1023.

KANE, I.A., CATTERALL, V., MCCAFFREY, W.D. & MARTINSEN, O.J. (2010) Submarine Channel Response to Intrabasinal Tectonics: The Influence of Lateral Tilt. *AAPG Bulletin*, **94,** 189-219.

KNELLER, B.C. & BRANNEY, M.J. (1995) Sustained High-Density Turbidity Currents and Deposition of Thick Massive Sands. *Sedimentology*, **42,** 607-616.

KOUTSOUVELI, A., METTOS, A., TSAPRALIS, V., TSAILA-MONOPOLI, S. & IOAKIM, C. (1989) Geological map of Greece: 1:50,000, Xylokastro Sheet. IGME Publications, Athens, Greece.

LEEDER, M.R. & GAWTHORPE, R.L. (1987) Sedimentary Models for Extensional Tilt-Block/Half-Graben Basins. In: *Continental Extensional Tectonics* (Ed. by Coward M. P., Dewey J. F. & Hancock P. L.) *Geological Society, London, Special Publications*, **28,** 139-152.

LEEDER, M.R., COLLIER, R.E.L., ABDUL AZIZ, L.H., TROUT, M., FERENTINOS, G., PAPATHEODOROU, G. & LYBERIS, E. (2002) Tectono-Sedimentary Processes Along an Active Marine/Lacustrine Half-Graben Margin: Alkyonides Gulf, E. Gulf of Corinth, Greece. *Basin Research*, **14,** 25-41.

LEEDER, M.R., PORTMAN, C., ANDREWS, J.E., COLLIER, R.E.L., FINCH, E., GAWTHORPE, R.L., MCNEILL, L.C., PEREZ-ARLUCEA, M. & ROWE, P.J. (2005) Normal Faulting and Crustal Deformation, Alkyonides Gulf and Perachora Peninsula, Eastern Gulf of Corinth Rift, Greece. *Journal of the Geological Society, London*, **162,** 549-561.

LEEDER, M.R., MACK, G.H., BRASIER, A.T., PARRISH, R.R., MCINTOSH, W.C., ANDREWS, J.E. & DUERMEIJER, C.E. (2008) Late-Pliocene Timing of Corinth (Greece) Rift-Margin Fault Migration. *Earth and Planetary Science Letters*, **274,** 132-141.

LEEDER, M.R., MARK, D.F., GAWTHORPE, R.L., KRANIS, H., LOVELESS, S., PEDENTCHOUK, N., SKOURTSOS, E., TURNER, J., ANDREWS, J.E. & STAMATAKIS, M. (2012) A "Great Deepening": Chronology of Rift Climax, Corinth Rift, Greece. *Geology*, **40,** 999-1002.

LEPPARD, C.W. & GAWTHORPE, R.L. (2006) Sedimentology of Rift Climax Deep Water Systems; Lower Rudeis Formation, Hammam Faraun Fault Block, Suez Rift, Egypt. *Sedimentary Geology*, **191,** 67-87.

LEWIS, K.B. (1971) Slumping on a Continental Slope Inclined at 1°- 4°. *Sedimentology*, **16,** 97-110.

LI, P., KNELLER, B.C., HANSEN, L. & KANE, I.A. (2016) The Classical Turbidite Outcrop at San Clemente, California Revisited: An Example of Sandy Submarine Channels with Asymmetric Facies Architecture. *Sedimentary Geology*, **346,** 1-16.

LUCENTE, C.C. & PINI, G.A. (2003) Anatomy and Emplacement Mechanism of a Large Submarine Slide within a Miocene Foredeep in the Northern Apennines, Italy: A Field Perspective. *American Journal of Science*, **303,** 565-602.

MAIER, K.L., BROTHERS, D.S., PAULL, C.K., MCGANN, M., CARESS, D.W. & CONRAD, J.E. (2017) Records of Continental Slope Sediment Flow Morphodynamic Responses to Gradient and Active Faulting from Integrated Auv and Rov Data, Offshore Palos Verdes, Southern California Borderland. *Marine Geology*, **393,** 47-66.

MAIER, K.L., ROLAND, E.C., WALTON, M.A.L., CONRAD, J.E., BROTHERS, D.S., DARTNELL, P. & KLUESNER, J.W. (2018) The Tectonically Controlled San Gabriel Channel–Lobe Transition Zone, Catalina Basin, Southern California Borderland. *Journal of Sedimentary Research*, **88,** 942-959.

MCARTHUR, A.D., KNELLER, B.C., WAKEFIELD, M.I., SOUZA, P.A. & KUCHLE, J. (2016) Palynofacies Classification of the Depositional Elements of Confined Turbidite Systems: Examples from the Gres D'annot, Se France. *Marine and Petroleum Geology*, **77,** 1254-1273.

MOERNAUT, J. & DE BATIST, M. (2011) Frontal Emplacement and Mobility of Sublacustrine Landslides: Results from Morphometric and Seismostratigraphic Analysis. *Marine Geology*, **285,** 29-45.

MORLEY, C.K., HARANYA, C., PHOOSONGSEE, W., PONGWAPEE, S., KORNSAWAN, A. & WANGANAN, N. (2004) Activation of Rift Oblique and Rift Parallel Pre-Existing Fabrics During Extension and Their Effect on Deformation Style: Examples from the Rifts of Thailand. *Journal of Structural Geology*, **26,** 1803-1829.

MORRIS, E.A., HODGSON, D.M., BRUNT, R.L. & FLINT, S.S. (2014) Origin, Evolution and Anatomy of Silt-Prone Submarine External Levées. *Sedimentology*, **61,** 1734-1763.

MOULIN, M., ASLANIAN, D. & UNTERNEHR, P. (2010) A new starting point for the South and Equatorial Atlantic Ocean, *Earth-Science Reviews*, **98,** 1–37.

MURAVCHIK, M., BILMES, A., D'ELIA, L. & FRANZESE, J.R. (2014) Alluvial Fan Deposition Along a Rift Depocentre Border from the Neuquén Basin, Argentina. *Sedimentary Geology*, **301,** 70-89.

MURAVCHIK, M., GAWTHORPE, R.L., SHARP, I.R., RARITY, F. & HODGETTS, D. (2018) Sedimentary Environment Evolution in a Marine Hangingwall Dipslope Setting. El Qaa Fault Block, Suez Rift, Egypt. *Basin Research*, **30,** 452-478.

NORMARK, W.R. (1978) Fan Valleys, Channels, and Depositional Lobes on Modern Submarine Fans: Characters for Recognition of Sandy Turbidite Environments. *AAPG Bulletin*, **62,** 912-931.

NORMARK, W.R., PIPER, D.J.W. & HESS, G.R. (1979) Distributary Channels, Sand Lobes, and Mesotopography of Navy Submarine Fan, California Borderland, with Applications to Ancient Fan Sediments. *Sedimentology*, **26,** 749-774.

NØTTVEDT, A., BERGE, A.M., DAWERS, N.H., FÆRSETH, R.B., HÄGER, K.O., MANGERUD, G. & PUIGDEFABREGAS, C. (2000) Syn-Rift Evolution and Resulting Play Models in the Snorre-H Area, Northern North Sea. In: *Dynamics of the Norwegian Margin* (Ed. by A. Nøttvedt), **167**, 179-218. Geological Society, London, Special Publication 167.

OLUBOYO, A.P., GAWTHORPE, R.L., BAKKE, K. & HADLER-JACOBSEN, F. (2014) Salt Tectonic Controls on Deep-Water Turbidite Depositional Systems: Miocene, Southwestern Lower Congo Basin, Offshore Angola. *Basin Research*, **26,** 597-620.

PAPATHEODOROU, G. & FERENTINOS, G. (1993) Sedimentation Processes and Basin-Filling Depositional Architecture in an Active Asymmetric Graben: Strava Graben, Gulf of Corinth, Greece. *Basin Research*, **5,** 235-253.

PEMBERTON, E.A.L., HUBBARD, S.M., FILDANI, A., ROMANS, B. & STRIGHT, L. (2016) The Stratigraphic Expression of Decreasing Confinement Along a Deep-Water Sediment Routing System: Outcrop Example from Southern Chile. *Geosphere*, **12,** 114-134.

PE-PIPER, G. & KOUKOUVELAS, I. (1990) Petrology and Geochemistry of Granitic Pebbles in the Pliocene Fluvial Deposits of the Northwest Peloponesse (Greece) and Their Regional Significance. *Neues Jahrbuch für Mineralogie - Abhandlungen*, **161,** 327-343.

PE-PIPER, G. & PIPER, D.J.W. (1991) Early Mesozoic Oceanic Subduction-Related Volcanic Rocks, Pindos Basin, Greece. *Tectonophysics*, **192,** 273-292.

PE-PIPER, G. & KOUKOUVELAS, I. (1992) Petrology, Geochemistry and Regional Significance of Igneous Clasts Pebbles in Parnassos Flysch, Amphissa Area, Greece. *Neues Jahrbuch für Mineralogie - Abhandlungen*, **164,** 94-112.

POSAMENTIER, H.W. & KOLLA, V. (2003) Seismic Geomorphology and Stratigraphy of Depositional Elements in Deep-Water Settings. *Journal of Sedimentary Research*, **73,** 367-388.

PRÉLAT, A., HODGSON, D.M. & FLINT, S.S. (2009) Evolution, Architecture and Hierarchy of Distributary Deep-Water Deposits: A High-Resolution Outcrop Investigation from the Permian Karoo Basin, South Africa. *Sedimentology*, **56,** 2132-2154.

PRÉLAT, A. & HODGSON, D.M. (2013) The Full Range of Turbidite Bed Thickness Patterns in Submarine Lobes: Controls and Implications. *Journal of the Geological Society*, **170,** 209-214.

RARITY, F., VAN LANEN, X.M.T., HODGETTS, D., GAWTHORPE, R.L., WILSON, P., FABUEL-PÉREZ, I. & REDFERN, J. (2014) Lidar-Based Digital Outcrops for Sedimentological Analysis: Workflows and Techniques. In: *Sediment-Body Geometry and Heterogeneity: Analogue Studies for Modelling the Subsurface* (Ed. by Martinius A. W., Howell J. A. & Good T. R.) *Geological Society, London, Special Publications*, **387,** 153-183.

RAVNÅS, R. & STEEL, R.J. (1997) Contrasting Styles of Late Jurassic Syn-Rift Turbidite Sedimentation: A Comparative Study of the Magnus and Oseberg Areas, Northern North Sea. *Marine and Petroleum Geology*, **14,** 417-449.

RAVNÅS, R. & STEEL, R.J. (1998) Architecture of Marine Rift-Basin Successions. *AAPG Bulletin*, **82,** 110-146.

RAVNÅS, R., NØTTVEDT, A., STEEL, R.J. & WINDELSTAD, J. (2000) Syn-Rift Sedimentary Architectures in the Northern North Sea. In: *Dynamics of the Norwegian Margin* (Ed. by Nøttvedt A.) *Geological Society, London, Special Publication*, **167,** 133–177.

ROHAIS, S., ESCHARD, R., FORD, M., GUILLOCHEAU, F. & MORETTI, I. (2007) Stratigraphic Architecture of the Plio-Pleistocene Infill of the Corinth Rift: Implications for Its Structural Evolution. *Tectonophysics*, **440,** 5-28.

SKOURTSOS, E., KRANIS, H., ZAMBETAKIS-LEKKAS, A., GAWTHORPE, R.L. & LEEDER, M. (2016) Alpine Basement Outcrops at Northern Peloponnesus: Implications for the Early Stages in the Evolution of the Corinth Rift. *Bulletin of the Geological Society of Greece*, **50,** 153-163.

SMITH, D.P. & BUSBY, C.J. (1993) Mid-Cretaceous Crustal Extension Recorded in Deep-Marine Half-Graben Fill, Cedros Island, Mexico. *Geological Society of America Bulletin*, **105,** 547-562.

SOHN, Y.K., KIM, S.B., HWANG, I.G., BAHK, J.J., CHOE, M.Y. & CHOUGH, S.K. (1997) Characteristics and Depositional Processes of Large-Scale Gravelly Gilbert-Type Foresets on the Miocene Doumsan Fan Delta, Pohang Basin, Se Korea. *Journal of Sedimentary Research*, **67,** 130-141.

SOHN, Y.K. (2000) Depositional Processes of Submarine Debris Flows in the Miocene Fan Deltas, Pohang Basin, Se Korea with Special Reference to Flow Transformation. *Journal of Sedimentary Research*, **70,** 491-503.

SPYCHALA, Y.T., HODGSON, D.M., STEVENSON, C.J. & FLINT, S.S. (2017) Aggradational Lobe Fringes: The Influence of Subtle Intrabasinal Seabed Topography on Sediment Gravity Flow Processes and Lobe Stacking Patterns. *Sedimentology*, **64,** 582-608.

STECKLER, M.S., BERTHELOT, F., LYBERIS, N. & LE PICHON, X. (1988) Subsidence in the Gulf of Suez: Implications for Rifting and Plate Kinematics. *Tectonophysics*, **153,** 249-270.

STEVENSON, C.J., JACKSON, C.A.L., HODGSON, D.M., HUBBARD, S.M. & EGGENHUISEN, J.T. (2015) Deep-Water Sediment Bypass. *Journal of Sedimentary Research*, **85,** 1058-1081.

STRACHAN, L.J., RARITY, F., GAWTHORPE, R.L., WILSON, P., SHARP, I.R. & HODGETTS, D. (2013) Submarine Slope Processes in Rift-Margin Basins, Miocene Suez Rift, Egypt. *Geological Society of America Bulletin*, **125,** 109-127.

SUMNER, E.J., TALLING, P.J., AMY, L.A., WYNN, R.B., STEVENSON, C.J. & FRENZ, M. (2012) Facies Architecture of Individual Basin-Plain Turbidites: Comparison with Existing Models and Implications for Flow Processes. *Sedimentology*, **59,** 1850-1887.

SYMONS, W.O., SUMNER, E.J., PAULL, C.K., CARTIGNY, M.J.B., XU, J.P., MAIER, K.L., LORENSON, T.D. & TALLING, P.J. (2017) A New Model for Turbidity Current Behavior Based on Integration of Flow Monitoring and Precision Coring in a Submarine Canyon. *Geology*, **45,** 367-370.

TATARIS, A., MARAGOUDAKIS, N., KOUNIS, G., CHRISTODOULOU, G. & TSAILA-MONOPOLI, S. (1970) Geological map of Greece: 1:50,000, Nemea Sheet. IGME Publications, Athens, Greece.

TALLING, P.J., MASSON, D.G., SUMNER, E.J. & MALGESINI, G. (2012) Subaqueous Sediment Density Flows: Depositional Processes and Deposit Types. *Sedimentology*, **59,** 1937-2003.

TORSVIK, T.H., ROUSSE, S., LABAILS, C. & SMETHURST, M.A. (2009) A new scheme for the opening of the South Atlantic Ocean and the dissection of an Aptian salt basin. *Geophysical Journal International*, **177,** 1315–1333.

TSOFLIAS, P. FLEURY, J.J. & IOAKIM, C. (1993) Geological map of Greece: 1:50,000, Derveni Sheet. IGME Publications, Athens, Greece.

WINN, R.D. & DOTT, R.H. (1979) Deep-Water Fan-Channel Conglomerates of Late Cretaceous Age, Southern Chile. *Sedimentology*, **26,** 203-228.

WYNN, R.B., KENYON, N.H., MASSON, D.G., STOW, D.A.V. & WEAVER, P.P.E. (2002) Characterization and Recognition of Deep-Water Channel-Lobe Transition Zones. *AAPG Bulletin*, **86,** 1441-1462.

ZHANG, X., SCHOLZ, C.A., HECKY, R.E., WOOD, D.A., ZAL, H.J. & EBINGER, C.J. (2014) Climatic Control of the Late Quaternary Turbidite Sedimentology of Lake Kivu, East Africa: Implications for Deep Mixing and Geologic Hazards. *Geology*, **42,** 811-814.

ZHANG, X. & SCHOLZ, C.A. (2015) Turbidite Systems of Lacustrine Rift Basins: Examples from the Lake Kivu and Lake Albert Rifts, East Africa. *Sedimentary Geology*, **325,** 177-191.

ZIEGLER, P.A. & CLOETHINGH, S. (2004) Dynamic Processes Controlling Evolution of Rifted Basins. *Earth-Science Reviews*, **64,** 1-50.

LIST OF FIGURES AND CAPTIONS

Fig. 1. Location maps. (A) Aegean/Mediterranean tectonic setting; red rectangle indicates the location of (B). (B) Corinth Rift regional map; red rectangle indicates the location of (C). (C) Geological map of the central Corinth Rift, modified from Gawthorpe *et al.* (2017b). Active faults are indicated in red and fossilised ones in black. The orientations of the depocentre main boundary fault systems are indicated with stereonet diagrams while the orientations of the faults internal to the depocentre are shown with a fault-plane pole distribution diagram. Pie diagrams show the results of clast composition analysis on different sources of sediment to the RDF such as deltas (Kyllini, Kefalari and Mavro) and intrabasinal highs with exposures of previous syn-rift units (Korfiotissa Formation, Ano Pitsa Formation and Pellini Formation). Ls: limestones, Ss: sedimentary rocks (mainly sandstones), Ps: phyllites, RC: red chert, BC: black chert, Gr: granitoids. The complete dataset used for the clast composition analysis is presented in the Supplementary data section.

Fig. 2. Study area in the Amphithea fault block. (A) Geological map. (B) Cross section B-B'. (C) Cross section C-C' with reconstructed stratigraphy above present day topography. The different stratigraphic units within the RDF are marked with numbered coloured circles (Fig. 3). The internal normal faults in the depocentre define fault blocks (FB) 1, 2, 3, 4 and 5. Note the occurrence of extensive slide sheets towards the northern sector of the Amphithea fault block.

Fig. 3. Stratigraphic column of the RDF in the Amphithea fault block (Fig. 2). The different units are numbered from 1 to 16 following their stratigraphic order. Note that the channel system represented by units 3, 7, 8 and 10 is laterally equivalent to units 1, 4, 5, 6 and 9. The entire interval depicted in this column corresponds to 615 m. Red arrow indicates the approximate position of the ash bed studied by Leeder *et al.* (2012).

Fig. 4. Basin-floor tilting events within the Amphithea depocentre (Fig. 2). (A) Schematic representation of the Amphithea fault block showing the relative position of the growth strata and angular unconformities measured in B, C, D, E and F. Diagram not to scale. (B) and (C) Limb rotation and growth-strata associated to the growth of the Amphithea fault found in Fault Block 4 (Fig. 2a). (B) Field photograph with indications of bedding dip and strike measured from a digital outcrop model. The bedding values indicated in green are represented in the stereonet diagram in C. Note the increase in thickness down-dip the monocline limb, from 15.4 to 18 m in the indicated interval (TST: true stratigraphic thickness). The expanded view shows stratal onlap up-dip onto the limb of the monocline. Field of view is approximately 250 m wide. (C) Stereonet diagram showing the direction of limb rotation. The bedding dip values decrease from 52° to 28° upwards in the stratigraphy of the growth-strata. This decrease in dip reflects the progressive rotation of the limb of the monocline developed on top of the blind Amphithea fault during its growth (Fig. 4A). The stereonet diagrams in D, E and F display plane values that represent the best fit plane for surfaces tracked along the extent of each fault block in the digital outcrop models: Unit 1 internal boundary (D) and the top boundaries of units 10 and 13 (D, E and F). The angular unconformity observed within Unit 1 is represented by the difference in dip between the measurements of units 1 and 10 (D) (Figs 2 and 3). The angular unconformity observed at the base of Unit 11 is represented by the difference in dip between the measurements of units 10 and 13 (D, E and F) (Figs 2 and 3). The unconformity at the base of Unit 11 cannot be measured properly in Fault Block 3 due to the quality of the exposures at that interval. The difference in the direction of tilt among fault blocks 1, 2 and 4 (D, E and F) shows the local effect of the internal growing normal faults over the larger-scale tilting experienced by the Amphithea hangingwall as a whole towards the NNE. Note that the red arrow in the stereonet diagrams only indicates the direction of tilting, but is not scaled to match its magnitude.

Fig. 5. Clast composition analysis. Diagrams show the proportion of the different clast lithologies expressed as percentages for depositional units within the RDF (A and C) and their possible sources (B, D and E). The lithologies of the clasts are grouped according to their provenance (*i.e.* Pindos and Tripolis units *vs*. Phyllites-Quartzites Unit). (A) Values measured in the conglomerate-dominated lobes, units 2, 4, 5, 12 and 15, have a great affinity to those registered for the Korfiotissa and Ano Pitsa formations (B). (C) In contrast, the values measured in the other type of units (e.g. units 3, 13

and 16) have a provenance akin to the one measured for the Mavro delta (D) and different from other sources of the RDF such as the Kyllini or Kefalari deltas (E). The complete dataset used for the clast composition analysis is presented in the Supplementary data section.

Fig. 6. Palaeotranport analysis of the RDF in the Amphithea fault block. (A, B and C) Rose diagrams of palaeotranport directions superposed to the fault plane pole distribution diagram for the faults internal to the Amphithea fault block (Fig. 1). (A) Palaeotranport directions measured in the conglomerate-dominated lobes (units 4, 5, 9, 12 and 15; indicated with numbered coloured circles on the rose diagram) (Figs 2 and 3). (B) Palaeotranport directions measured in all other units found below the ~6° angular unconformity (units 1, 3, 7, 8 and 10) (Figs 2 and 3). (C) Palaeotranport directions measured in all other units found above the ~6° angular unconformity (units 11, 13, 14, and 16) (Figs 2 and 3). (D) Palaeotransport data plotted according to the size of the measured directional features (lobe axes, channel thalwegs, scours, current ripples, and trough-cross stratification). The size of the circles is scaled to represent the cross sectional area (m^2) of the directional features measured in this study. Note that the majority of the measured features are thicker than 1 m and larger than 5 m in length.

Fig. 7. Main characteristics of the different types of depositional elements recognised in the RDF exposed in the Amphithea fault block. Box sketches represent the architectural style of each element. The corresponding sedimentary logs (Fig. 8) are indicated on each sketch. Grain-size proportions in the rock bodies are shown as percentage values represented by pie diagrams. Cgl: conglomerates, I-Cgl: intraclast conglomerates, Ss: sandstones, Ms: mudstones. P-Q: Phyllites-Quartzites Unit.

Fig. 8. Representative sedimentary log sections for each type of depositional element (Fig. 7). (A) and (B) Type A, mudstone-dominated sheets (A) and their sandstone enriched intervals (B). (C) Type B, conglomerate-dominated lobes. (D) and (E) Type C, conglomerate channel belts (D) and sandstone sheets (E). (F) and (G) Type D, sandstone channel belts: channel fill (F) and overbank deposits (G). (H) Type E, sandstone-dominated broad shallow lobes. (I) Type F, sandstone-dominated sheets with broad shallow channels. The UTM coordinates of the log sections are as follows: (A) 636781 E, 4213508 N; (B) 638733 E, 4213144 N; (C) 638749 E, 4213236 N; (D) 638730 E, 4212505 N; (E) 638829 E, 4212376 N; (F) 638823 E, 4212574 N; (G) 638761 E, 4212529 N; (H) 638819 E, 4212595 N; (I) 638753 E, 4213159 N.

Fig. 9. Field photographs of depositional unit type A. (A) Cliff exposures of alternating mudstone-dominated sheets in Unit 1. Intervals enriched in sandstone beds that appear intercalated can be laterally traced until they link with the exposures of the channel system (units 3, 7, 8 and 10; Fig. 3). The black rectangle indicates the location of Fig. 9f. (B) Centimetre-thick intercalations of tabular

mudstones and sandstones. (C) Plant fragments at the base of the beds. (D) Bioturbation extending from the sandstone laminae into the mudstone intervals. (E) Conglomerate lens with 2 to 3 cm clasts supported in a fine to medium sandstone matrix. (F) Tapering wedges occur at the termination of the sandstone enriched intervals in Unit 1. These aggradational features are interpreted to represent the fringes of the internal units in the channel system (units 3, 7, 8 and 10; Fig. 3) interdigitated with Unit 1. Field of view is approximately 100 m wide. The location of the wedge is indicated with a black rectangle in Fig. 9a.

Fig. 10. Field photographs of depositional element type B. (A) Lobate body with convex top and relatively flat base. Sitting person circled for scale. Field of view is approximately 100 m wide. (B) Marlstone dike injected at the base of the lobe in A. (C) Tabular matrix-supported conglomerate beds. Conglomerates are supported by a sandstone matrix. (D) Conglomerate beds 20 to 90 cm thick intercalated with 10 to 30 cm thick lenses of laminated fine to coarse sandstones subjected to intense soft-sediment normal faulting. Note that the highly irregular geometry of the bedding mimics the configuration of the small-scale faulting (grabens and halfgrabens) and neither channels nor scours are found among these conglomerates.

Fig. 11. Field photographs of the channel system exposed at the Riza hill (Fig. 2a). (A) Aerial view of the Riza hill. (B) Distribution of the internal units in the channel system (units 3, 7, 8 and 10; Fig. 3) and their boundaries. White rectangles indicate the relative location of the pictures in C, D, E and F. (C) Depositional element type C: conglomerate-dominated channel belts in Unit 3. (D) Depositional element type D: southwestern margin of a channel element in Unit 7. (E) Depositional element type E: sandstone-dominated lobe in Unit 8. (F) Depositional element type F deposits: sandstone-dominated succession with shallow channels in Unit 10.

Fig. 12. Field photographs of depositional element type C (A, B, C and D), type D (E, F and G) and type E (H and I). (A) Tabular conglomerate beds intercalated with laminated sandstones. (B) Poorly sorted grain- to matrix-supported conglomerate with sandstone matrix. (C) Conglomerates rich in sandstone and mudstone intraclasts (2 to 30 cm in length) in deposits at the lower half of a channel belt. (D) Decimetre thick sandstone beds intercalating thinner, centimetre thick, rippled sandstones and mudstones found external to the channel belts. Ruler (circled) on the right-hand side is 1 m in length. (E and F) Concentration of intraclasts at the margins of a channel element in Unit 7 (depositional element type D). (G) Deposits external to the channel belts in Unit 7 (depositional element type D). Tabular sandstone beds with ripples on top interbedded with laminated mudstones and rippled siltstones. (H) Evidence of erosion at the base of a body of coarse to very coarse sandstones and fine pebble-grade conglomerates. (I) Fine to medium sandstone beds 15 to 30 cm thick intercalated with 2 to 5 cm thick intervals of mudstones and very fine rippled sandstones.

Fig. 13. Depositional element type F. (A) Aerial view of Unit 13. Coloured circles indicate the different units in the cliff section (Fig. 3). (B) Rippled siltstones and sandstones intercalated with marlstone laminae. (C) Typical sandstone channel containing sandstone and mudstone intraclasts. (D) Two vertically amalgamated sandstone lenses. A grain-supported conglomerate is found at the base of the upper lens (indicated with white arrows). (E) Unrooted isoclinally-folded sandstone intraclast towards the top of a mudstone-supported tabular deposit towards the base of Unit 13.

Fig. 14. Slide sheets towards the top of the RDF in the Amphithea fault block (Figs 2 and 3). Vergence of the thrusted slide sheets is towards northeast. (A) Field photograph and line interpretation (B). Selected marker intervals are indicated with green, blue and red colours. Pictures in (A) and (B) taken from 639109 E, 4214709 N. The orientation of the fault ramps and flats in the thrust sheets was measured from the digital outcrop models from LiDAR and photogrammetry and restored according to the Amphithea fault block regional dip and dip direction: (C) rose diagram of fault strike and (D) fault plane poles density distribution and its principal stresses orientation ($\sigma 1$: maximum, $\sigma 2$: intermediate and $\sigma 3$: minimum). Note that the strike of the thrusts parallels that of the northern and southern fault boundary systems in the Amphithea fault block (E) (Figs 1 and 2). (F) and (G) Sketches illustrating the development of the slide sheets in the Amphithea fault block. (G) Continuous tilting of the hangingwall towards the NE led to oversteepening of overpressurised deposits in units 14 and 16. Major and minor detachments were thus generated, over which sheets slid to the NE, following the topographic gradient (G). Stacking of the slide sheets resulted in their thrusting with a NE vergence. Note that the diagrams in (F) and (G) are not to scale and proportions are exaggerated for better visualization.

Fig. 15. Tectono-sedimentary models of the evolution of the RDF depositional environment in the Amphithea fault block. View towards the west. Representation of the northern margin of the basin is schematic and only for illustrative purposes. Numbered coloured circles correspond to the different stratigraphic units identified in this study (Figs 2 and 3). Base level (lake/marine) is kept constant throughout the models. (A, B, and C) Deposition below the ~6° angular unconformity. Development of an axial channel system (units 3, 7, 8 and 10) fed from the Mavro delta and funnelled between the Amphithea and Xylokastro highs on a basin floor plain (Unit 1). Subordinately, a transverse system consisting of conglomerate-dominated lobes (units 2, 4, 5, 6, 9) is sourced from the Xylokastro high. Different stages in the evolution of the channel system are illustrated for the deposition of conglomerate channel belts and sandstone sheets (A), sandstone channel belts (B) and sandstone-dominated sheets with broad shallow channels (D). (B) Tilting of the Amphithea hangingwall block towards the NNE occurs from a combination of the accrued displacement in the northern border and the growing faults at the southern border. Fine-grained deposition becomes dominant (Unit 11). There

are presently no evidences that any channel system such as the one in (A) existed for this stage. Nevertheless, it is possible that the channel system migrated closer to the northern fault border following the north-eastwards basin floor gradient caused by the tilting of the hangingwall and its deposits lie present-day in the subsurface. (C) Deposition of a sandstone-dominated sheet with broad shallow channels (Unit 13) sourced from the Mavro delta and conglomerate-dominated lobes (Unit 12) sourced from the Xylokastro high. (D) A new phase of fine grained deposition (Unit 14) dominates the Amphithea hangingwall. Occasionally, conglomerate-dominated lobes (Unit 15) sourced from the Xylokastro high reach the basin floor. (E) Renewed deposition of a sandstone-dominated sheet with broad shallow channels (Unit 16) sourced from the Mavro delta. (F) Continuous tilting of the Amphithea fault block generated gravitational instabilities that triggered large-scale landslides containing sheets of units 14 and 16. These slide sheets thrusted each other as they moved downslope and stacked in a complex of NE vergence on the northern half of the depocentre. The palaeotranport direction of the channel system below the ~6° angular unconformity (A, B and C) is towards the SE, perpendicular to the internal faults in the Amphithea fault block (Fig. 6b), whereas for the units above that unconformity (B, C, D and E) their palaeotransport directions are orientated towards the NE, parallel to the strike of these internal faults (Fig. 6c).

Figure 1

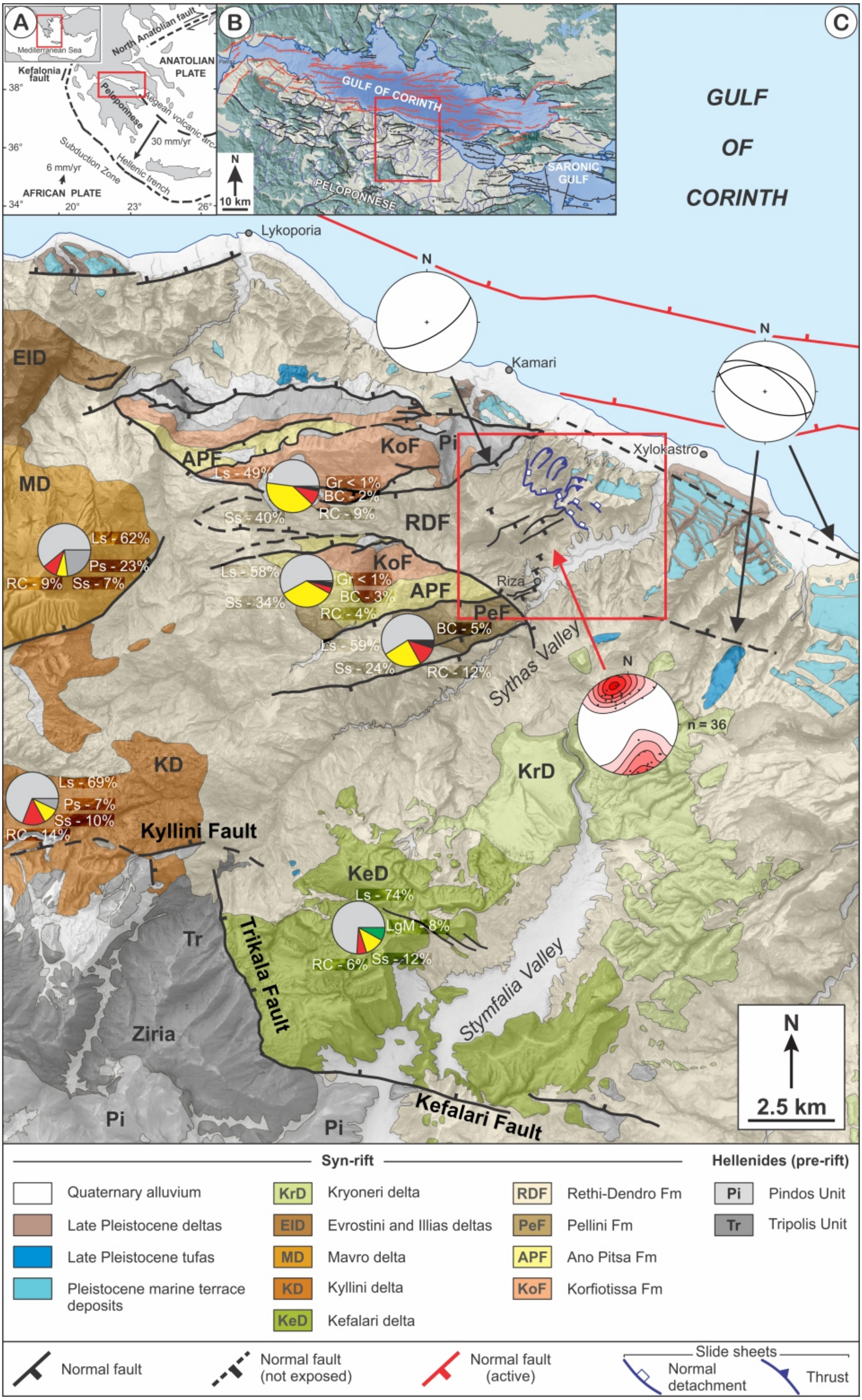

A
B
C
Mediterranean Sea
North Anatolian fault
ANATOLIAN PLATE
Kefalonia fault
Peloponnese
Aegean volcanic arc
30 mm/yr
Subduction Zone
Hellenic trench
6 mm/yr
AFRICAN PLATE
GULF OF CORINTH
SARONIC GULF
PELOPONNESE
10 km
GULF OF CORINTH
Lykoporia
Kamari
Xylokastro
Riza
EID
MD
KD
APF
KoF
Pi
RDF
PeF
KrD
KeD
Tr
Ziria
Pi
Sythas Valley
Stymfalia Valley
Kyllini Fault
Trikala Fault
Kefalari Fault
n = 36
Ls - 49%
Gr < 1%
BC - 2%
RC - 9%
Ss - 40%
Ls - 62%
Ps - 23%
RC - 9%
Ss - 7%
Ls - 58%
Gr < 1%
BC - 3%
RC - 4%
Ss - 34%
BC - 5%
Ls - 59%
Ss - 24%
RC - 12%
Ls - 69%
Ps - 7%
Ss - 10%
RC - 14%
Ls - 74%
LgM - 8%
RC - 6%
Ss - 12%
2.5 km
Syn-rift
Hellenides (pre-rift)
Quaternary alluvium
Late Pleistocene deltas
Late Pleistocene tufas
Pleistocene marine terrace deposits
KrD Kryoneri delta
EID Evrostini and Illias deltas
MD Mavro delta
KD Kyllini delta
KeD Kefalari delta
RDF Rethi-Dendro Fm
PeF Pellini Fm
APF Ano Pitsa Fm
KoF Korfiotissa Fm
Pi Pindos Unit
Tr Tripolis Unit
Normal fault
Normal fault (not exposed)
Normal fault (active)
Slide sheets
Normal detachment
Thrust

Figure 2

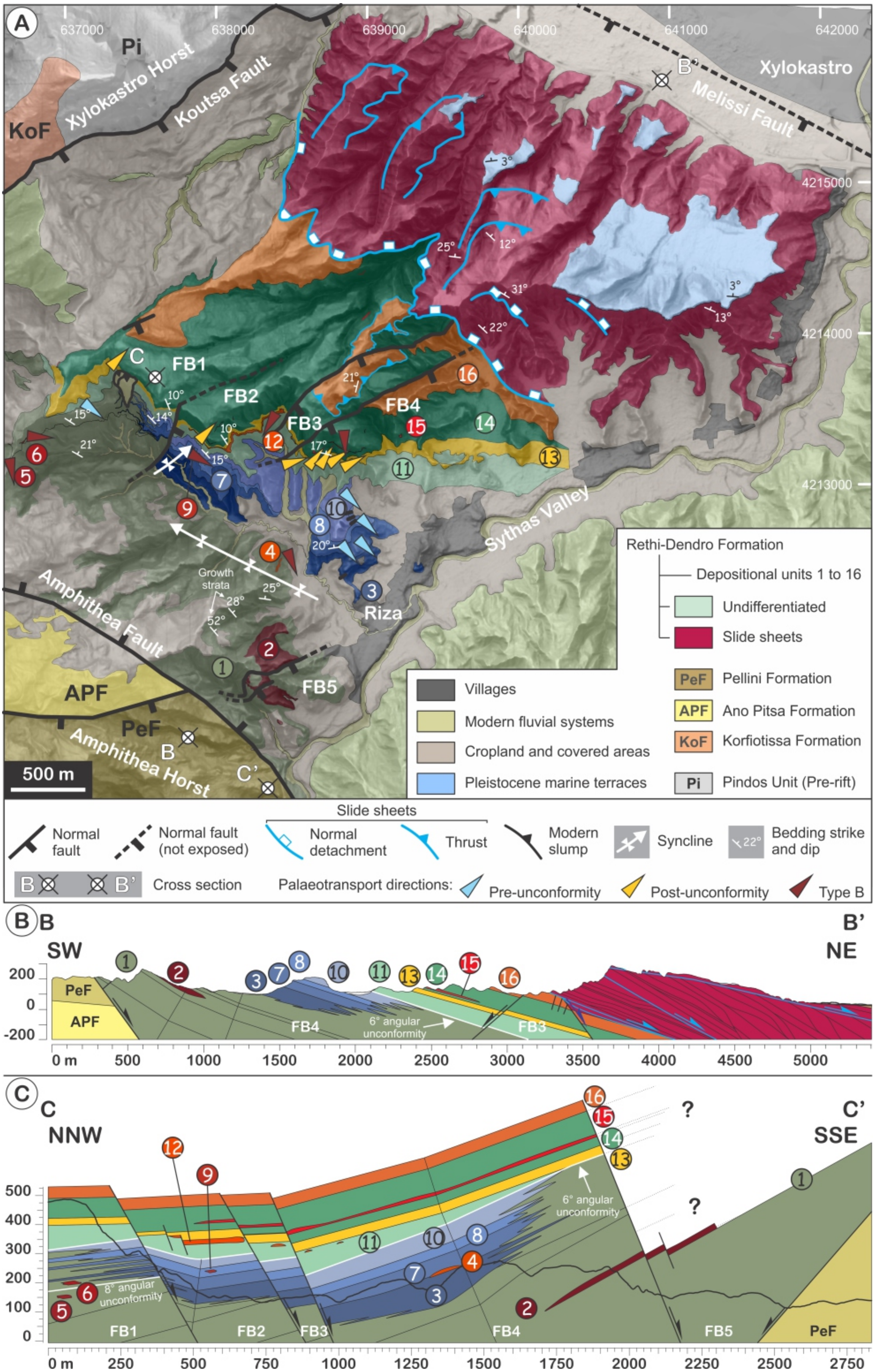

A
Pi
Xylokastro Horst
Koutsa Fault
KoF
Xylokastro
Melissi Fault
B'
FB1
FB2
FB3
FB4
FB5
C
Sythas Valley
Riza
Growth strata
Amphithea Fault
APF
PeF
B
C'
Amphithea Horst
500 m
Rethi-Dendro Formation
Depositional units 1 to 16
Undifferentiated
Slide sheets
PeF Pellini Formation
APF Ano Pitsa Formation
KoF Korfiotissa Formation
Pi Pindos Unit (Pre-rift)
Villages
Modern fluvial systems
Cropland and covered areas
Pleistocene marine terraces
Slide sheets
Normal fault
Normal fault (not exposed)
Normal detachment
Thrust
Modern slump
Syncline
Bedding strike and dip
Cross section
Palaeotransport directions:
Pre-unconformity
Post-unconformity
Type B
B
SW
NE
6° angular unconformity
C
NNW
SSE
8° angular unconformity

Figure 3

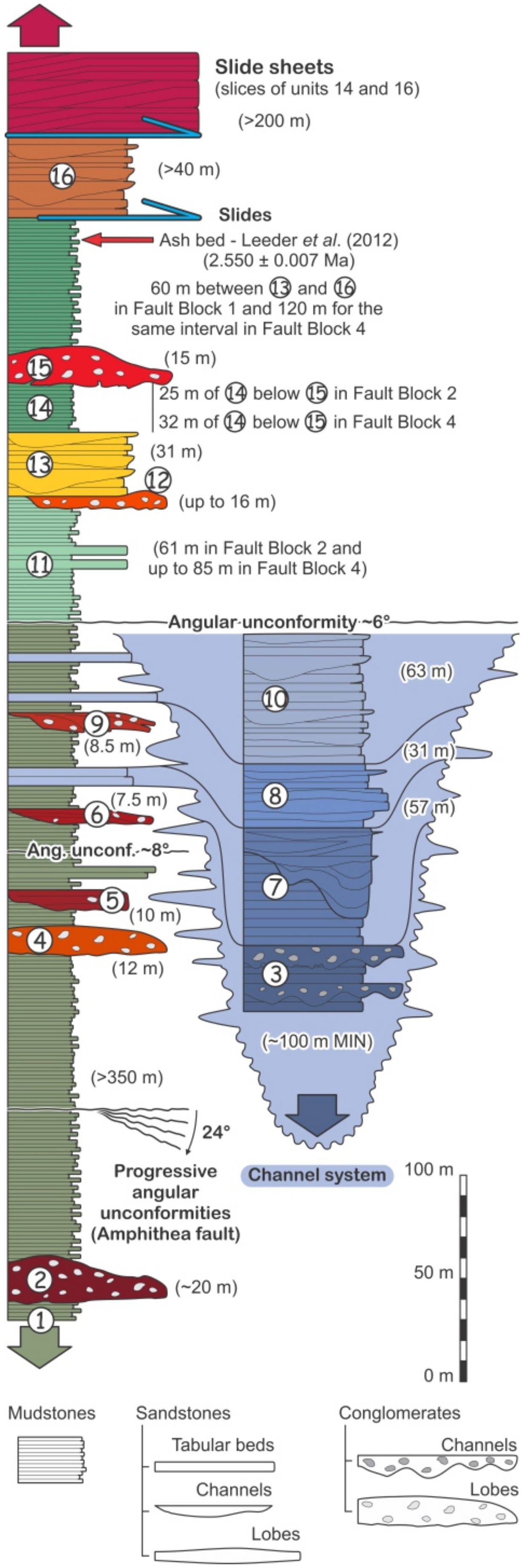

Slide sheets
(slices of units 14 and 16)
(>200 m)
16
(>40 m)
Slides
Ash bed - Leeder *et al.* (2012)
(2.550 ± 0.007 Ma)
60 m between 13 and 16
in Fault Block 1 and 120 m for the
same interval in Fault Block 4
15
(15 m)
14
25 m of 14 below 15 in Fault Block 2
32 m of 14 below 15 in Fault Block 4
13
(31 m)
12
(up to 16 m)
11
(61 m in Fault Block 2 and
up to 85 m in Fault Block 4)
Angular unconformity ~6°
10
(63 m)
9
(8.5 m)
(31 m)
8
(57 m)
6
(7.5 m)
Ang. unconf. ~8°
7
5
(10 m)
4
(12 m)
3
(~100 m MIN)
(>350 m)
24°
Progressive
angular
unconformities
(Amphithea fault)
Channel system
100 m
50 m
0 m
2
(~20 m)
1
Mudstones
Sandstones
Tabular beds
Channels
Lobes
Conglomerates
Channels
Lobes

Figure 4

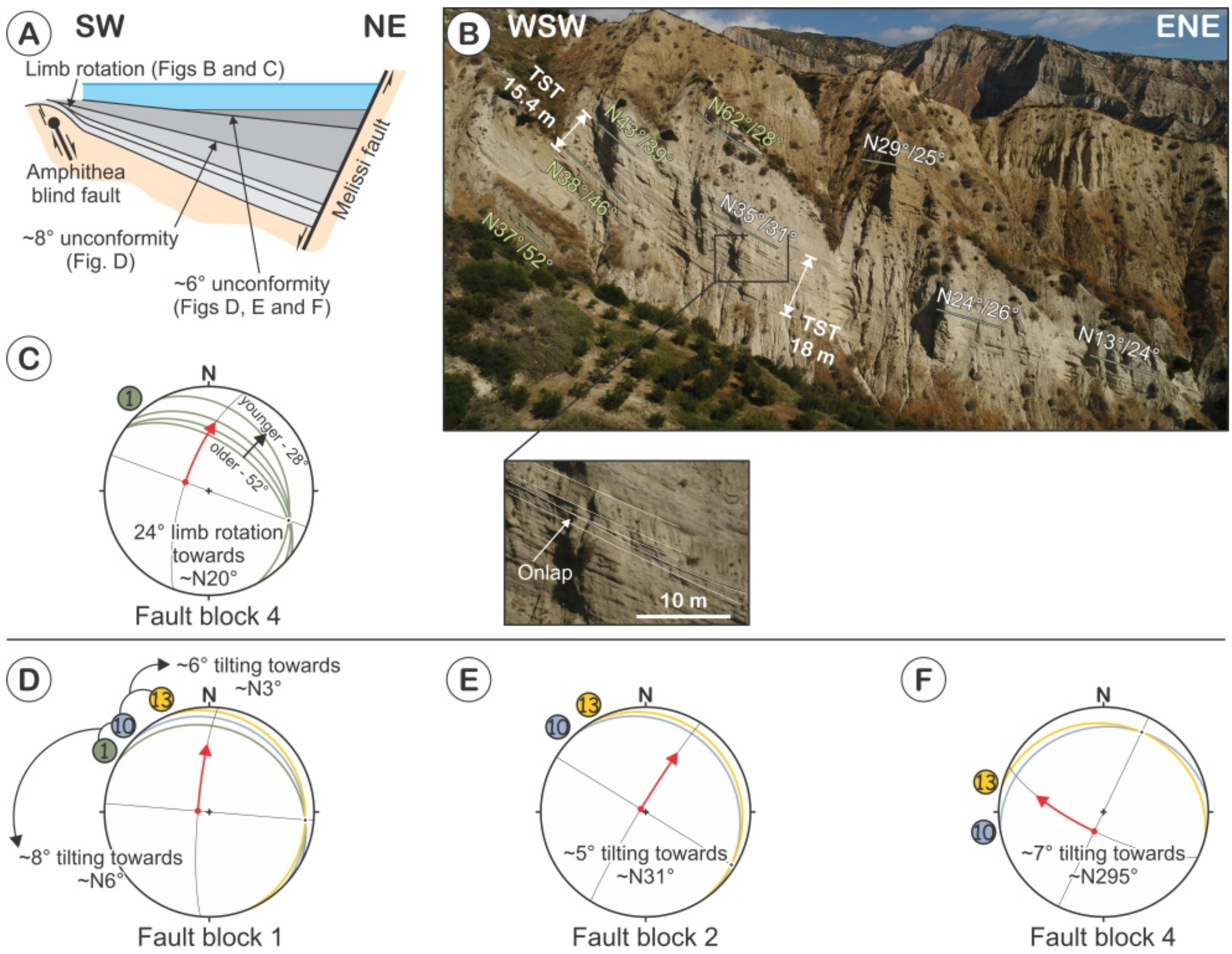

A
SW
NE
Limb rotation (Figs B and C)
Amphithea
blind fault
~8° unconformity
(Fig. D)
~6° unconformity
(Figs D, E and F)
Melissi fault
B
WSW
ENE
TST
15.4 m
N43°/39°
N62°/28°
N38°/46°
N37°/52°
N29°/25°
N35°/31°
TST
18 m
N24°/26°
N13°/24°
Onlap
10 m
C
N
1
younger - 28°
older - 52°
24° limb rotation
towards
~N20°
Fault block 4
D
~6° tilting towards
~N3°
13
10
1
N
~8° tilting towards
~N6°
Fault block 1
E
13
10
N
~5° tilting towards
~N31°
Fault block 2
F
N
13
10
~7° tilting towards
~N295°
Fault block 4

Figure 5

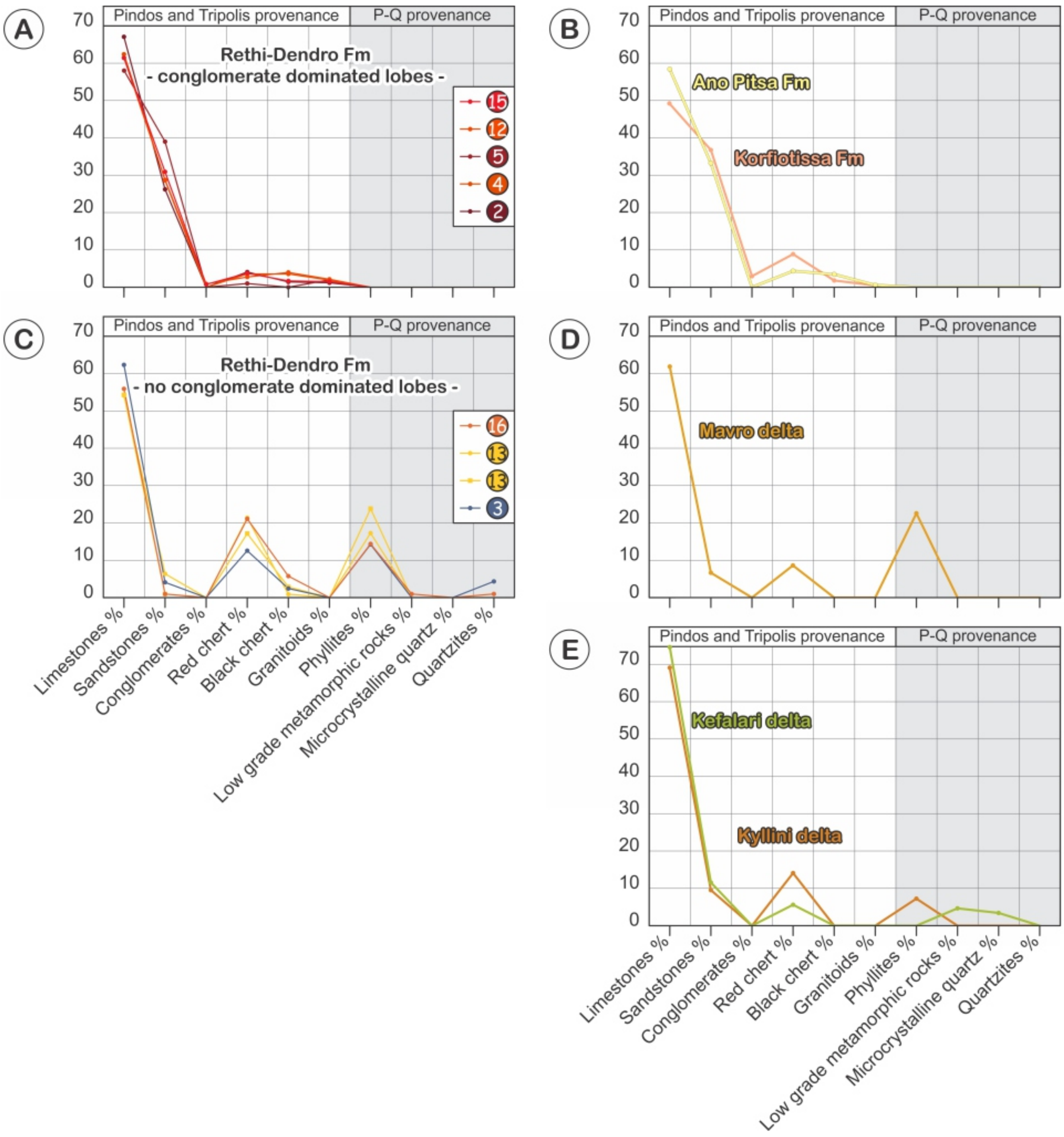
A
Pindos and Tripolis provenance
P-Q provenance
Rethi-Dendro Fm
- conglomerate dominated lobes -
15
12
5
4
2
B
Ano Pitsa Fm
Korfiotissa Fm
C
Rethi-Dendro Fm
- no conglomerate dominated lobes -
16
13
13
3
D
Mavro delta
E
Kefalari delta
Kyllini delta
70
60
50
40
30
20
10
0
Limestones %
Sandstones %
Conglomerates %
Red chert %
Black chert %
Granitoids %
Phyllites %
Low grade metamorphic rocks %
Microcrystalline quartz %
Quartzites %

Figure 6

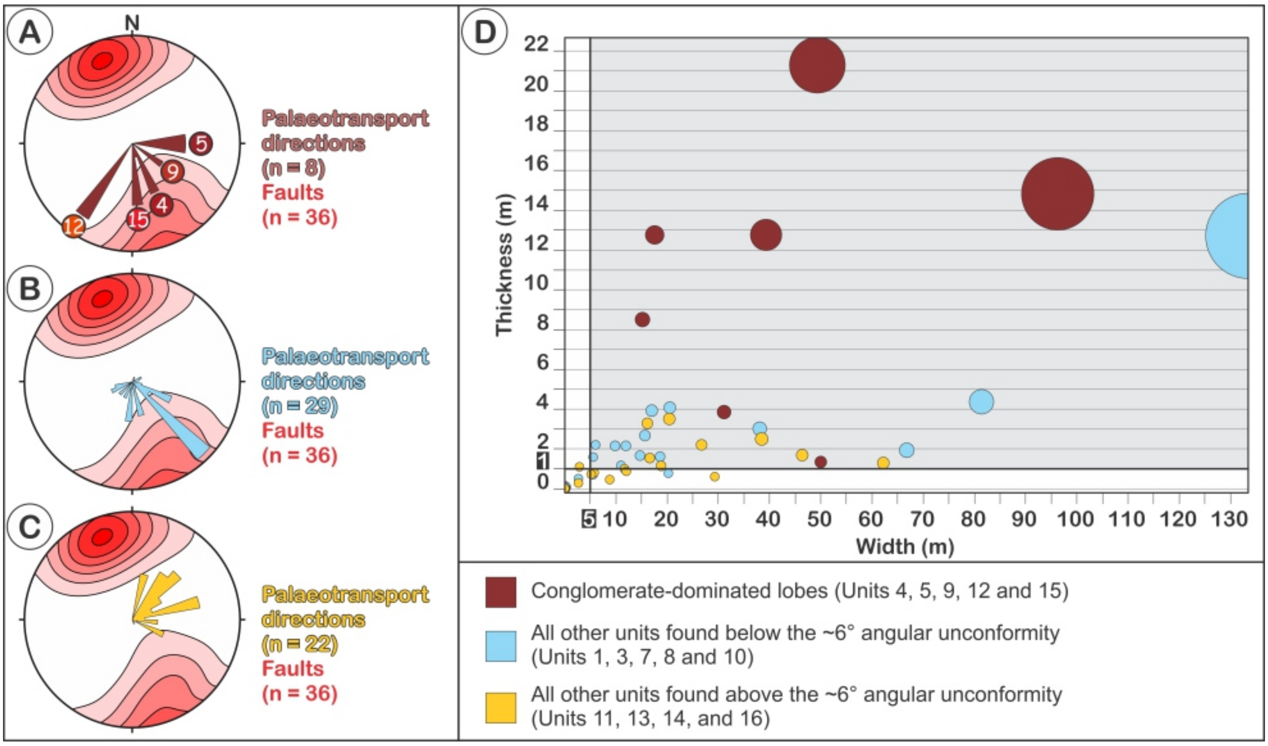

A
N
Palaeotransport directions
(n = 8)
Faults
(n = 36)
5
9
4
15
12
B
Palaeotransport directions
(n = 29)
Faults
(n = 36)
C
Palaeotransport directions
(n = 22)
Faults
(n = 36)
D
Thickness (m)
22
20
18
16
14
12
10
8
6
4
2
1
0
5
10
20
30
40
50
60
70
80
90
100
110
120
130
Width (m)
Conglomerate-dominated lobes (Units 4, 5, 9, 12 and 15)
All other units found below the ~6° angular unconformity (Units 1, 3, 7, 8 and 10)
All other units found above the ~6° angular unconformity (Units 11, 13, 14, and 16)

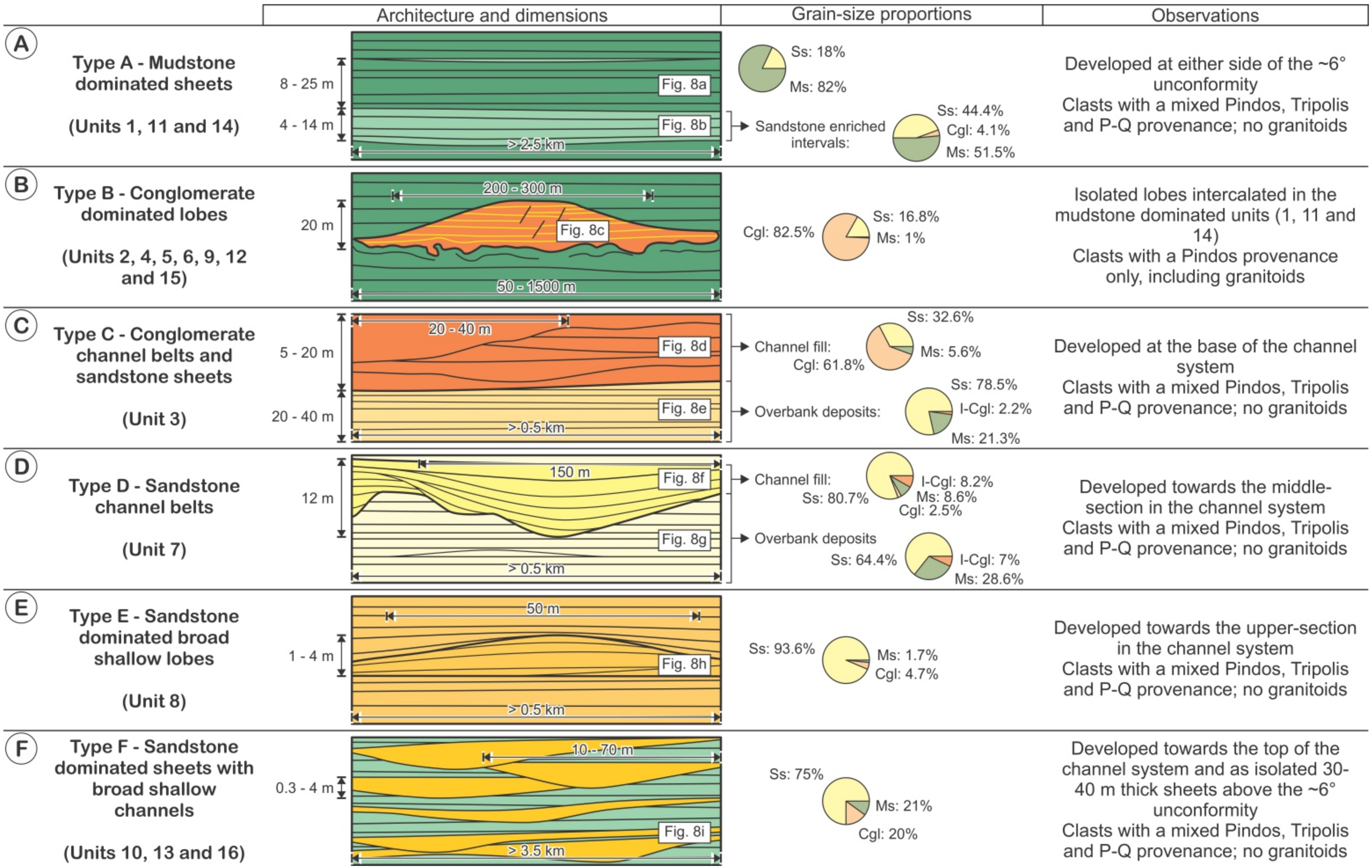
Architecture and dimensions
Grain-size proportions
Observations
A
Type A - Mudstone dominated sheets
(Units 1, 11 and 14)
8 - 25 m
4 - 14 m
> 2.5 km
Fig. 8a
Fig. 8b
Ss: 18%
Ms: 82%
Sandstone enriched intervals:
Ss: 44.4%
Cgl: 4.1%
Ms: 51.5%
Developed at either side of the ~6° unconformity
Clasts with a mixed Pindos, Tripolis and P-Q provenance; no granitoids
B
Type B - Conglomerate dominated lobes
(Units 2, 4, 5, 6, 9, 12 and 15)
20 m
200 - 300 m
50 - 1500 m
Fig. 8c
Cgl: 82.5%
Ss: 16.8%
Ms: 1%
Isolated lobes intercalated in the mudstone dominated units (1, 11 and 14)
Clasts with a Pindos provenance only, including granitoids
C
Type C - Conglomerate channel belts and sandstone sheets
(Unit 3)
5 - 20 m
20 - 40 m
20 - 40 m
> 0.5 km
Fig. 8d
Fig. 8e
Channel fill:
Cgl: 61.8%
Ss: 32.6%
Ms: 5.6%
Overbank deposits:
Ss: 78.5%
I-Cgl: 2.2%
Ms: 21.3%
Developed at the base of the channel system
Clasts with a mixed Pindos, Tripolis and P-Q provenance; no granitoids
D
Type D - Sandstone channel belts
(Unit 7)
12 m
150 m
> 0.5 km
Fig. 8f
Fig. 8g
Channel fill:
Ss: 80.7%
I-Cgl: 8.2%
Ms: 8.6%
Cgl: 2.5%
Overbank deposits
Ss: 64.4%
I-Cgl: 7%
Ms: 28.6%
Developed towards the middle-section in the channel system
Clasts with a mixed Pindos, Tripolis and P-Q provenance; no granitoids
E
Type E - Sandstone dominated broad shallow lobes
(Unit 8)
1 - 4 m
50 m
> 0.5 km
Fig. 8h
Ss: 93.6%
Ms: 1.7%
Cgl: 4.7%
Developed towards the upper-section in the channel system
Clasts with a mixed Pindos, Tripolis and P-Q provenance; no granitoids
F
Type F - Sandstone dominated sheets with broad shallow channels
(Units 10, 13 and 16)
0.3 - 4 m
10 - 70 m
> 3.5 km
Fig. 8i
Ss: 75%
Ms: 21%
Cgl: 20%
Developed towards the top of the channel system and as isolated 30-40 m thick sheets above the ~6° unconformity
Clasts with a mixed Pindos, Tripolis and P-Q provenance; no granitoids

Figure 7

Figure 8

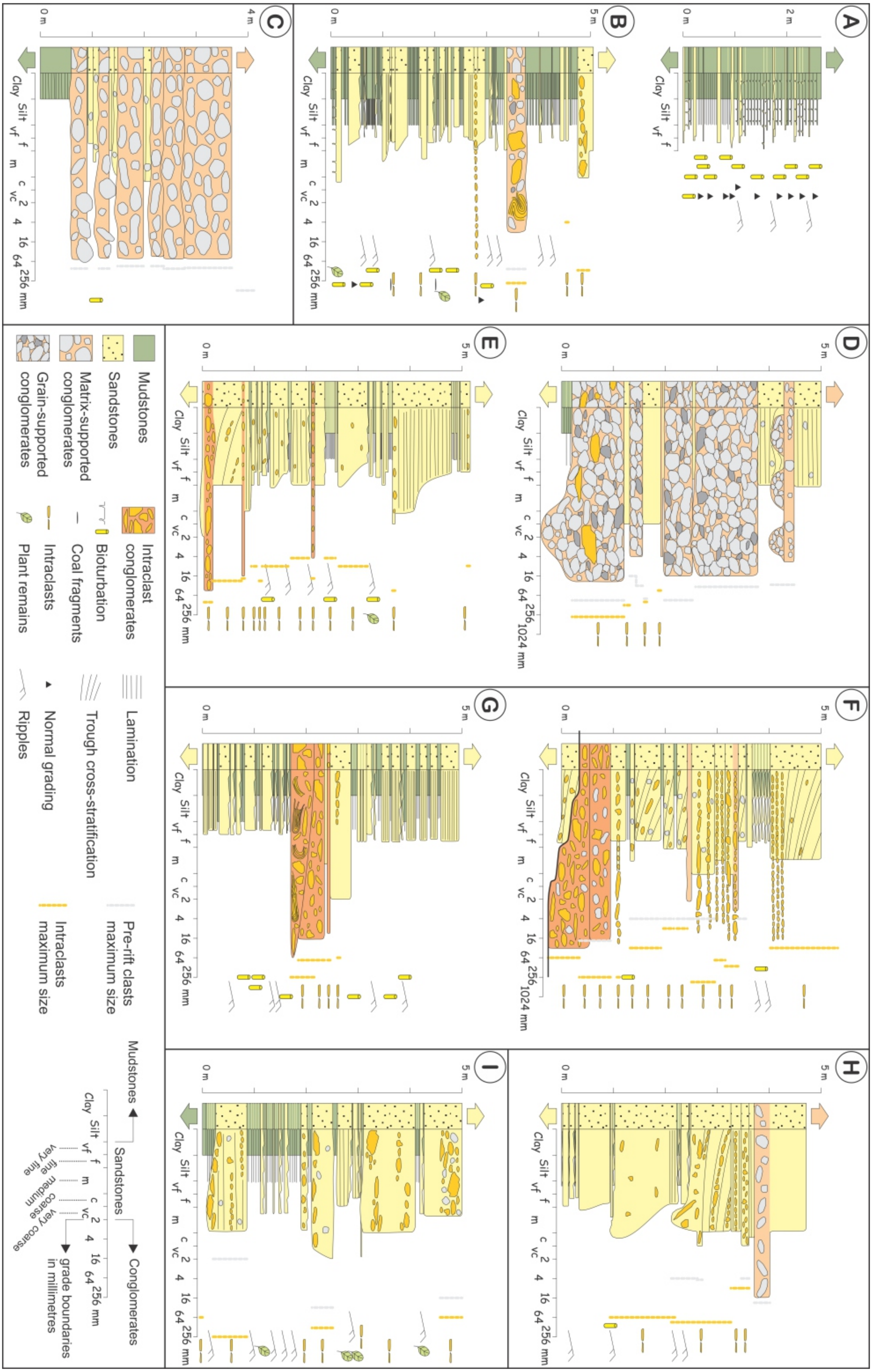

A
B
C
D
E
F
G
H
I
Clay Silt vf f m c vc 2 4 16 64 256 mm
Mudstones
Sandstones
Matrix-supported conglomerates
Grain-supported conglomerates
Intraclast conglomerates
Bioturbation
Coal fragments
Intraclasts
Plant remains
Lamination
Trough cross-stratification
Normal grading
Ripples
Pre-rift clasts maximum size
Intraclasts maximum size
Conglomerates
very fine
medium
very coarse
grade boundaries in millimetres

Figure 9

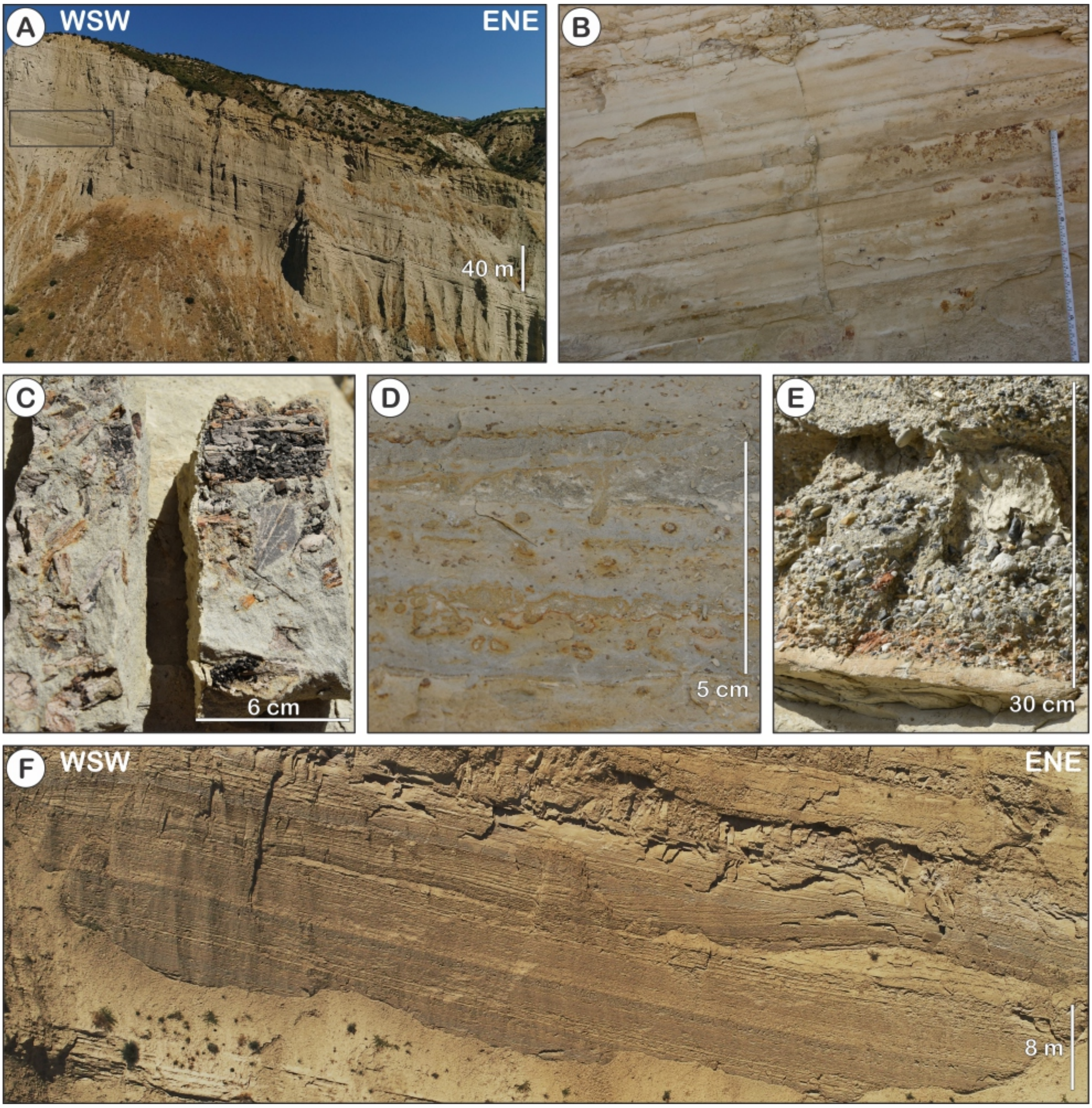

Figure 10

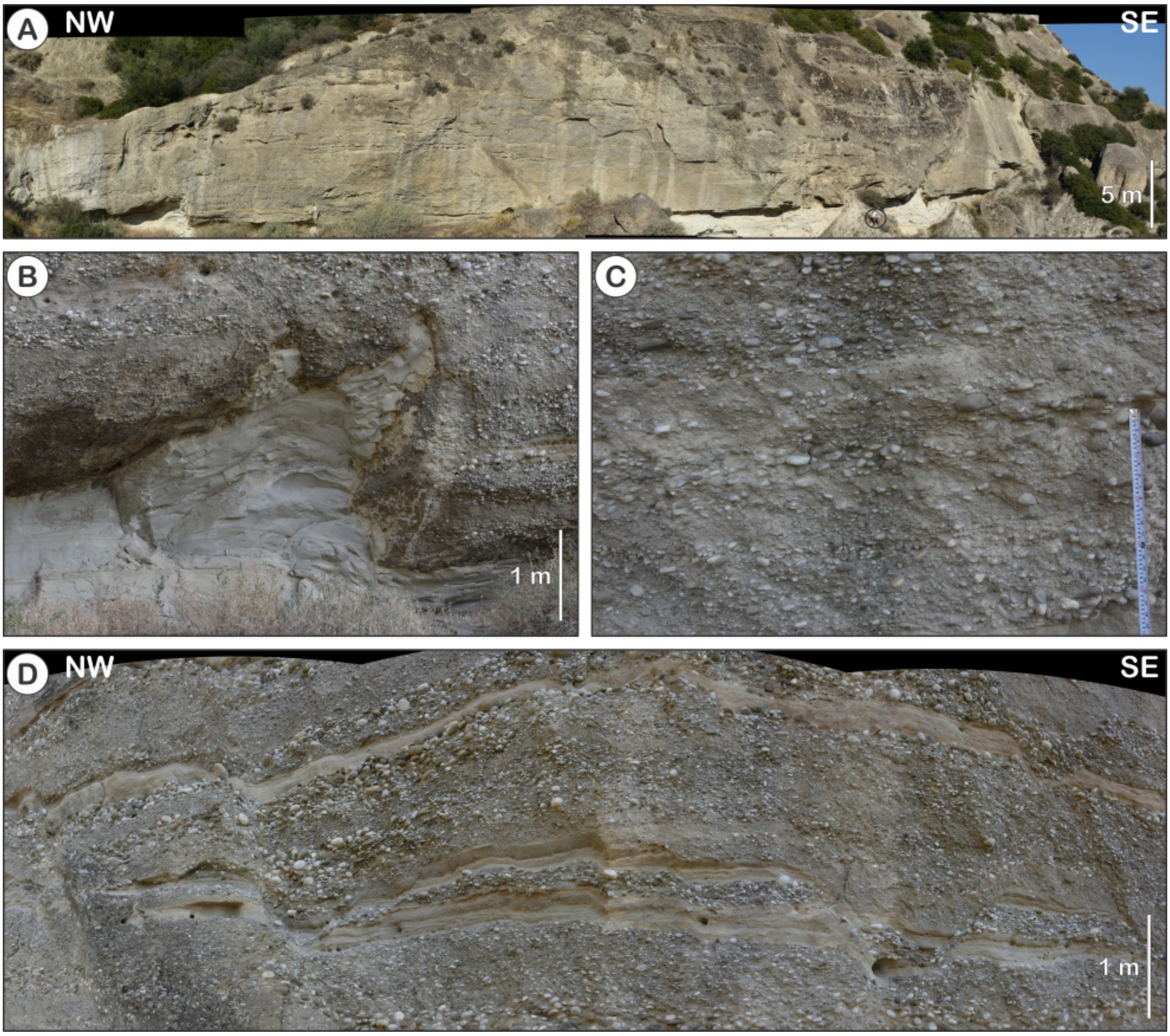

Figure 11

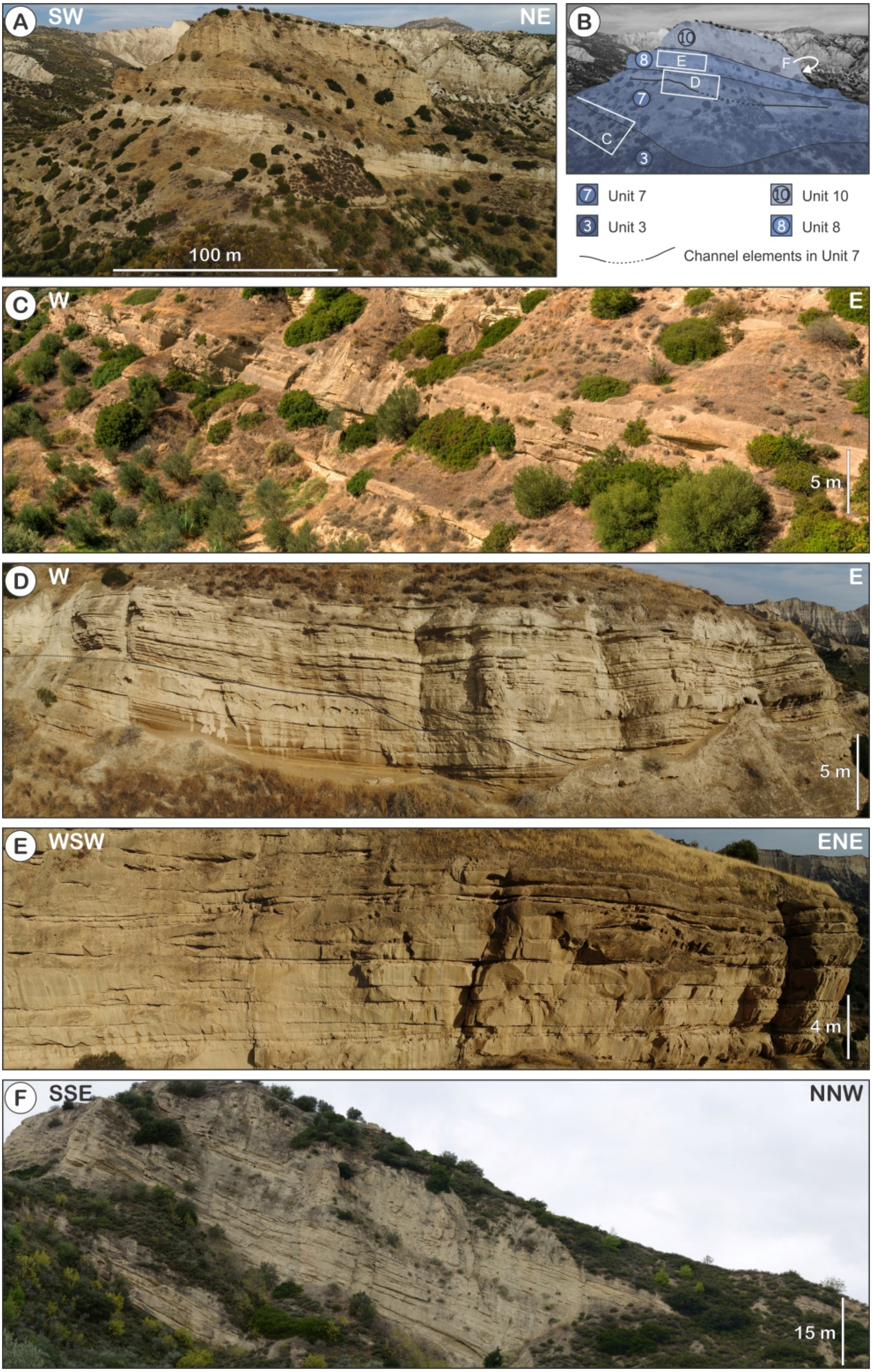

A
SW
NE
100 m
B
10
8
E
F
D
7
C
3
7 Unit 7
10 Unit 10
3 Unit 3
8 Unit 8
Channel elements in Unit 7
C
W
E
5 m
D
W
E
5 m
E
WSW
ENE
4 m
F
SSE
NNW
15 m

Figure 12

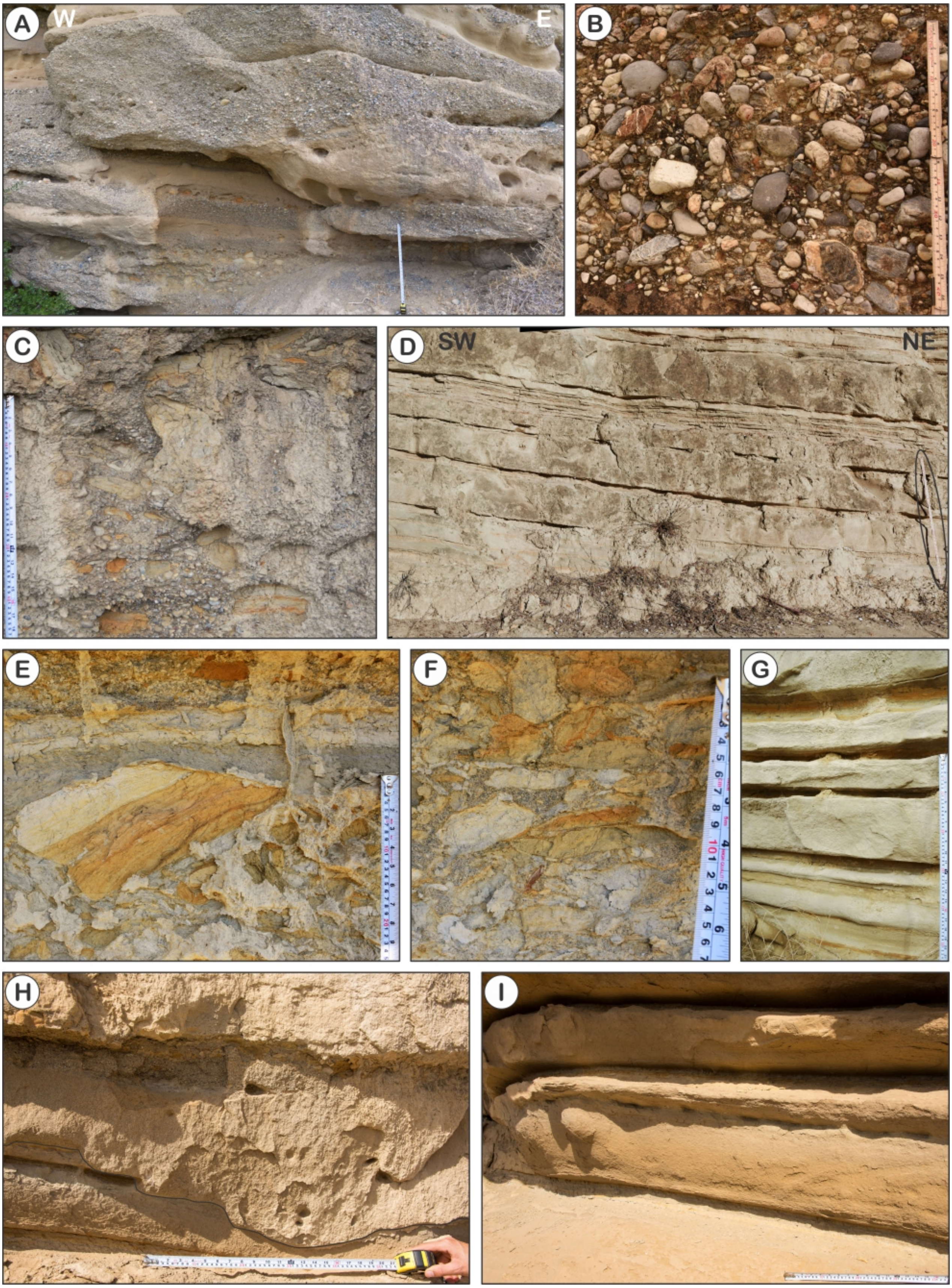

Figure 13

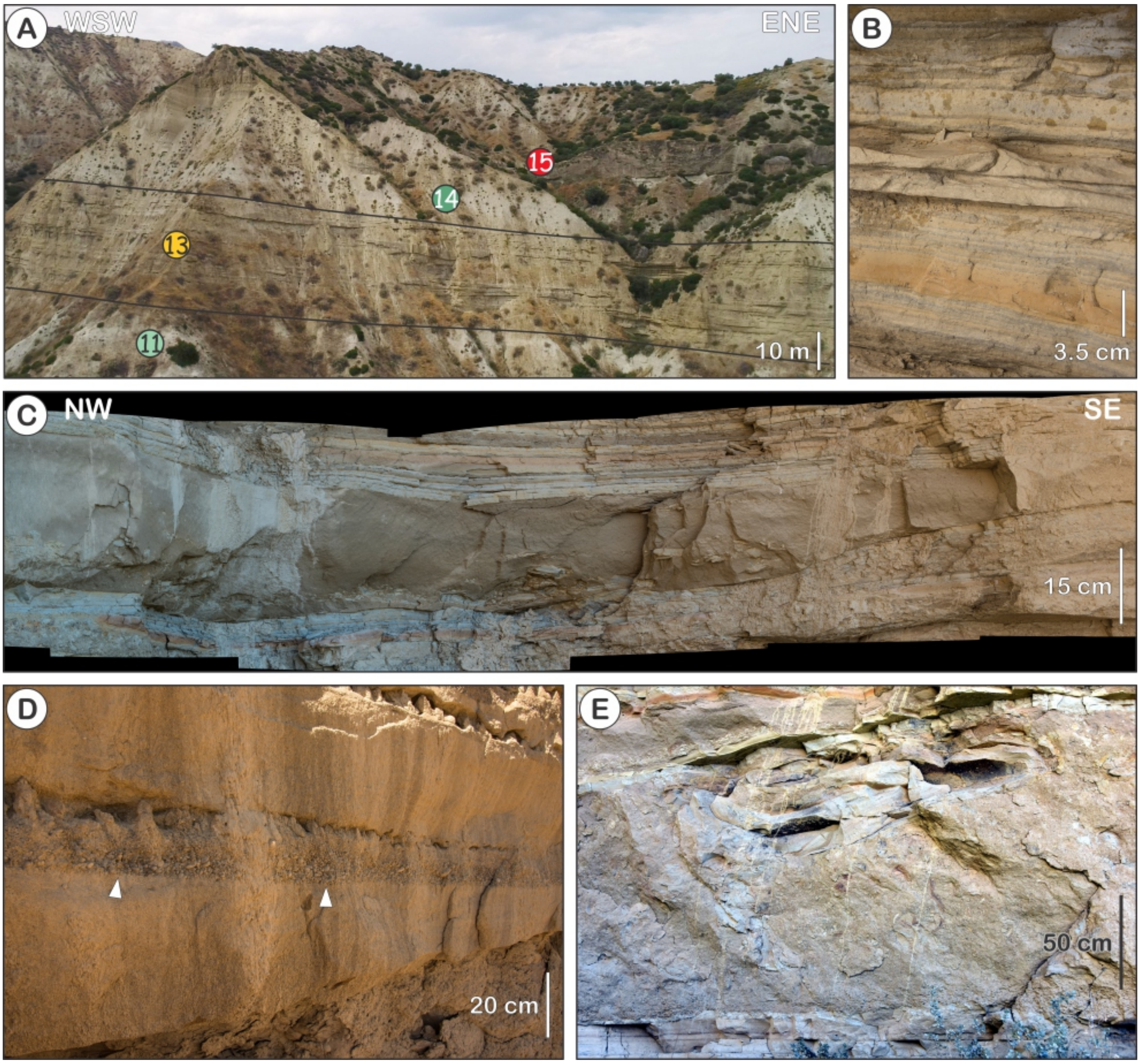

Figure 14

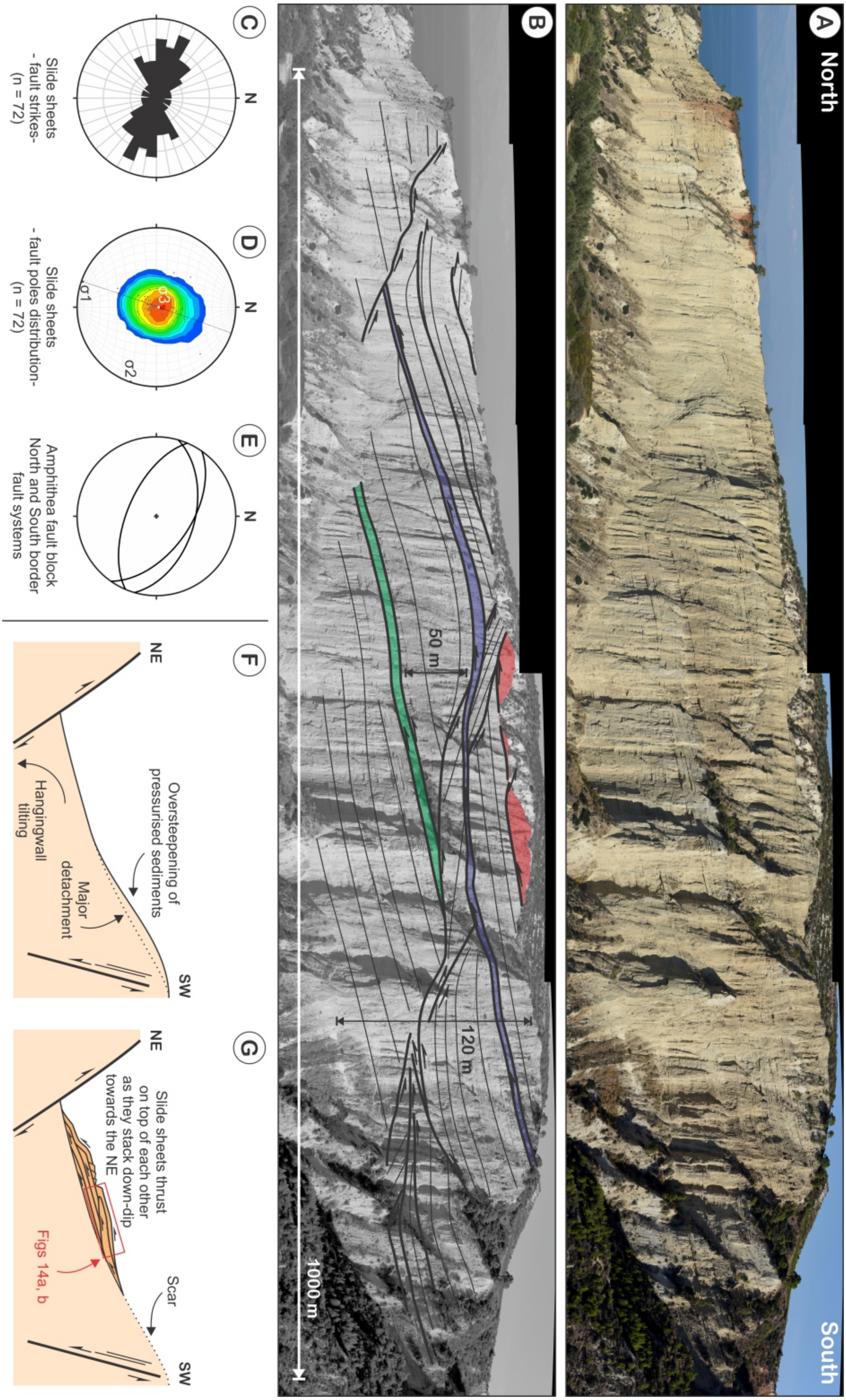

A
North
South
B
50 m
120 m
1000 m
C
N
Slide sheets
- fault strikes-
(n = 72)
D
N
σ1
σ2
σ3
Slide sheets
- fault poles distribution-
(n = 72)
E
N
Amphithea fault block
North and South border
fault systems
F
NE
SW
Oversteepening of
pressurised sediments
Major
detachment
Hangingwall
tilting
G
NE
SW
Slide sheets thrust
on top of each other
as they stack down-dip
towards the NE
Scar
Figs 14a, b

Figure 15

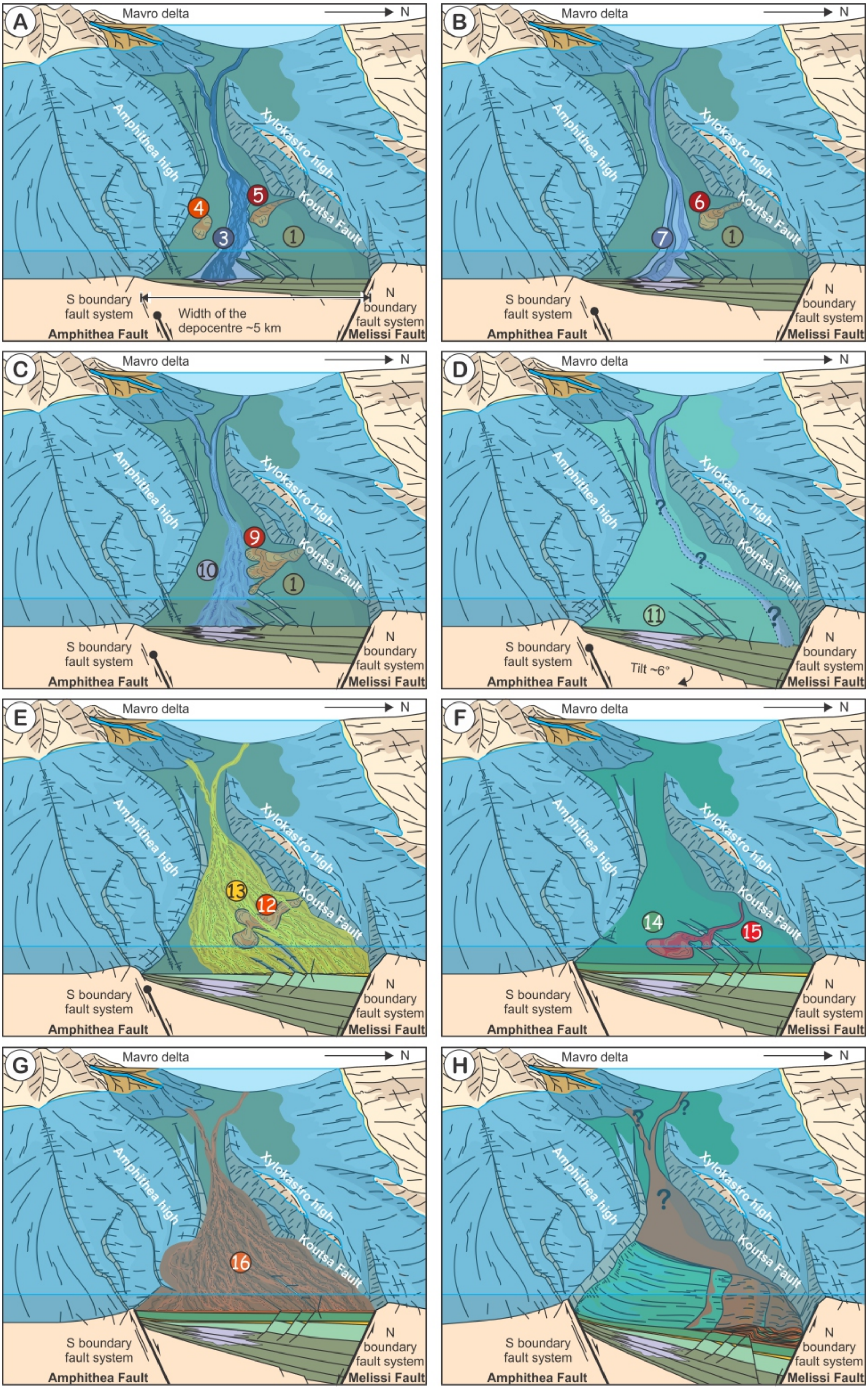
A
B
C
D
E
F
G
H
Mavro delta
N
Amphithea high
Xylokastro high
Koutsa Fault
S boundary
fault system
Amphithea Fault
N
boundary
fault system
Melissi Fault
Width of the
depocentre ~5 km
Tilt ~6°
1
3
4
5
6
7
9
10
11
12
13
14
15
16
?